

Response of a plate in turbulent channel flow: Analysis of fluid-solid coupling

Sreevatsa Anantharamu^a, Krishnan Mahesh^{a,*}

^aAerospace Engineering and Mechanics, University of Minnesota - Twin Cities, Minneapolis, MN 55455, USA

ARTICLE INFO

Keywords:

Direct numerical simulation
Fluid-structure interaction
Fluid-solid coupling
Plate vibration
Turbulent channel flow
Spectral POD
One-way coupling

ABSTRACT

The paper performs simulation of a rectangular plate excited by turbulent channel flow at friction Reynolds numbers of 180 and 400. The fluid-structure interaction is assumed to be one-way coupled, i.e, the fluid affects the solid and not vice versa. We solve the incompressible Navier Stokes equations using finite volume direct numerical simulation in the fluid domain. In the solid domain, we solve the dynamic linear elasticity equations using a time-domain finite element method. The obtained plate averaged displacement spectra collapse in the low frequency region in outer scaling. However, the high frequency spectral levels do not collapse in inner units. This spectral behavior is reasoned using theoretical arguments. We further study the sources of plate excitation using a novel formulation. This formulation expresses the average displacement spectra of the plate as an integrated contribution from the fluid sources within the channel. Analysis of the net displacement source reveals that at the plate natural frequencies, the contribution of the fluid sources to the plate excitation peaks in the buffer layer. The corresponding wall-normal width is found to be $\approx 0.75\delta$. We analyze the decorrelated features of the sources using spectral Proper Orthogonal Decomposition (POD) of the net displacement source. We enforce the orthogonality of the modes in an inner product with a symmetric positive definite kernel. The dominant spectral POD mode contributes to the entire plate excitation. The contribution of the remaining modes from the different wall-normal regions undergo destructive interference resulting in zero net contribution. The envelope of the dominant mode further shows that the location and width of the contribution depend on inner and outer units, respectively.

1. Introduction

The coupling between a turbulent flow and the resulting structural excitation is a problem of interest in marine, civil and aerospace engineering. In this paper, we investigate this coupling in a canonical setting - linear one-way coupled (fluid affects solid, but not vice versa) response of an elastic plate in turbulent channel flow (Pope, 2001) due to wall-pressure fluctuations alone. Specifically, we address the question - how much do the fluid sources at different wall-normal locations contribute to plate excitation for different frequencies, and what are the salient features of these fluid sources? We answer this question with a novel formulation that combines Direct Numerical Simulation (DNS) data, Green's function formulation and spectral Proper Orthogonal Decomposition (POD). For brevity, we will sometimes refer to wall-pressure fluctuations as just wall-pressure.

The one-way coupling between the fluid sources and plate excitation can be broken into two parts: i) fluid source - wall-pressure fluctuation coupling, and ii) wall-pressure fluctuation - plate excitation coupling. Note that we neglect the wall-shear stress contribution to the plate forcing. We further classify the techniques to investigate the fluid source - wall-pressure fluctuation coupling into - scaling variables-based, Green's function-based and conditional averaging-based techniques. We discuss some features of the wall-pressure fluctuation sources identified by each of these techniques.

Identification of the scaling variables for the power-spectral density (PSD) / wavenumber spectrum of wall-pressure fluctuation yields qualitative information of the wall-normal region of the fluid sources. The wall-pressure PSD in the low ($\omega\delta/u_\tau < 5$), mid ($5 < \omega\delta/u_\tau < 100$) and high frequency ranges ($\omega\delta/u_\tau > 0.3Re_\tau$) scale with the potential flow variables (ρ_f, δ^*, U_o), outer flow variables (ρ_f, δ, τ_w), and inner flow variables (ρ_f, ν, τ_w), respectively (Farabee and Casarella, 1991), where ω is the angular frequency, ρ_f is the fluid density, δ is the boundary layer thickness, δ^* is the displacement thickness of the boundary layer, U_o is the centerline velocity, τ_w is the wall-shear stress, $u_\tau = \sqrt{\tau_w/\rho_f}$

*Corresponding author

 anant035@umn.edu (S. Anantharamu); kmahesh@umn.edu (K. Mahesh)

ORCID(s):

is the friction velocity, and the friction Reynolds number Re_τ is defined as $u_\tau \delta / \nu_f$. Thus, the sources responsible for the low, mid and high frequency wall-pressure fluctuations are predominantly in the potential, outer and inner region of the turbulent boundary layer, respectively.

The Green's function-based techniques (Chang III, Piomelli and Blake, 1999; Anantharamu and Mahesh, 2019) yield quantitative information of the sources of wall-pressure fluctuation. The premultiplied streamwise wavenumber spectrum and the PSD of the wall-pressure fluctuations in a turbulent channel show peaks at $\lambda_x^+ = 300$ (Panton, Lee and Moser, 2017) and $\omega^+ \approx 0.35$ (Hu, Morfey and Sandham, 2006) for $Re_\tau = 180 - 5000$, respectively, where λ_x is the streamwise wavelength, and $+$ indicates normalization with viscous units (ν and u_τ). The dominant contributors to this inner peak are in the buffer region of the channel (Anantharamu and Mahesh, 2019). The approach of Anantharamu and Mahesh (2019) that identified this dominant contribution i) combines DNS data with the Green's function formulation to express the wall-pressure PSD ($\phi_{pp}(\omega)$) as integrated contribution ($\Gamma(r, s, \omega)$) from all wall-parallel plane pairs, $\phi_{pp}(\omega) = \iint_{-\delta}^{+\delta} \Gamma(r, s, \omega) dr ds$, ii) accounts for the relative phase difference between the contributions from different wall-parallel planes neglected in the previous Green's function approach of Chang III et al. (1999), and iii) yields a distribution of sources in the wall-normal direction instead of a wall-normal region as indicated by the scaling variables. Further, the methodology identified decorrelated features of wall-pressure fluctuation sources using spectral POD. The identified dominant wall-pressure source at the linear and premultiplied wall-pressure PSD peak frequency resembled tall and inclined patterns, respectively.

The conditional averaging-based technique (Ghaemi and Scarano, 2013) yield patterns of the flow structure responsible that are correlated to a particular wall-pressure fluctuation event. The time history of the wall-pressure fluctuation signal at a point on the wall shows occasional positive and negative high amplitude wall-pressure peaks. The conditionally averaged flow fields show coupling between a hairpin vortex and the high amplitude peaks (Ghaemi and Scarano, 2013). The flow structure responsible for the positive and negative high amplitude wall-pressure peak at a point are the sweep and ejection event occurring above it, respectively. The ejection event responsible for the negative peak occurs upstream of the hairpin head in between the quasi-streamwise vortices. The sweep event that leads to the positive peak occurs downstream of the hairpin head.

The dynamic linear elasticity equations describe the wall-pressure fluctuation - plate excitation coupling. This one-way coupled FSI approach is valid for small linear deformation ($du_\tau / \nu_f < 1$) of the plate, where d is the wall-normal displacement. The approach generally uses i) plate theories (e.g. Poisson Kirchoff) to describe the deformation, and modal superposition to obtain the response, ii) frequency domain since steady state response is usually the quantity of interest, and iii) a model wavenumber-frequency spectrum (Corcos, 1964; Chase, 1980; Hwang, 1998) for the spatially homogenous wall-pressure fluctuations as input. Note that the model wavenumber-frequency spectrum usually requires a model PSD (Bull, 1967; Smol' Iakov and Tkachenko, 1991; Goody, 2004). The mode shapes and natural frequencies of the plate required to perform modal superposition can be obtained analytically for simple boundary conditions and geometry. For complicated boundary conditions and geometry, Finite Element Method (FEM) is used to compute the modal decomposition.

The wall-pressure fluctuation - plate excitation coupling has been previously investigated in wavenumber space (Hwang and Maidanik, 1990; Blake, 2017). The modal force PSD of the plate can be expressed as the wavenumber integral (Blake, 2017)

$$\begin{aligned} \phi_{f_j f_j}(\omega) &= \iint_{-\infty}^{+\infty} \phi_{pp}(k_1, k_3, \omega) |S_j(k_1, k_3)|^2 dk_1 dk_3, \\ S_j(k_1, k_3) &= \int_a^{a+L_x} \int_b^{b+L_z} S_j(x, z) e^{i(k_1 x + k_3 z)} dx dz, \end{aligned} \quad (1)$$

where a and b are the origins of the plate in the streamwise and spanwise directions, L_x and L_z are the lengths of the plate in the streamwise and spanwise directions, $\phi_{f_j f_j}(\omega)$ is the modal force PSD of the j^{th} mode shape, $\phi_{pp}(k_1, k_3, \omega)$ is the wall-pressure wavenumber-frequency spectrum and $|S_j(k_1, k_3)|^2$ is the modal shape function. From the above equation, we observe that the modal shape function couples the wall-pressure wavenumber-frequency spectrum to the modal force. The relative contribution of different wavenumber regions to the modal force spectra depends on the mode order (j), boundary conditions, and the ratio of the streamwise modal wavenumber ($k_{m,j}$) to the convective wavenumber at the natural frequency of the mode (Hwang and Maidanik, 1990). The high streamwise wavenumber ($k_1 / k_{m,j} \gg 1$) portion of $|S_j(k_1, k_3)|^2$ decays as k_1^{-6} , k_1^{-4} and k_1^{-2} for clamped, simply supported and free boundary conditions on all edges (Blake, 2017). Thus, plates with free boundary conditions accept more of the high streamwise wavenumber

component of the wall-pressure fluctuations. Further, special wall-pressure fluctuation models that separately approximate the high and low wavenumber portion of the wall-pressure fluctuation wavenumber-frequency spectrum can be derived and used to obtain the response of plates (Hambric, Hwang and Bonness, 2004). Hambric et al. (2004) showed good agreement between FEM response of a plate excited by the modified Corcos model of Hwang (1998) and an equivalent edge forcing model which only models the convective component in the modified Corcos model for a plate with three edges clamped and one edge free. This shows the importance of the convective region of wall-pressure fluctuation spectrum for plates with free boundary conditions. For a plate with all four edges clamped, FEM response from a low wavenumber excitation model showed good agreement with the modified Corcos model, thus highlighting the dominance of low wavenumber contribution for clamped boundary condition.

Experiments by Zhang, Wang, Blake and Katz (2017) have shown coupling between flow structures and the response of a compliant wall in a turbulent channel flow. The large positive and negative deformation of the compliant wall is coupled to the ejection and sweep events, respectively, occurring above it (Zhang et al., 2017). Conditionally averaged flow fields show that these events are related to the high amplitude pressure peaks and hairpin vortices that surround the local deformation of the compliant wall. For large deformation of the compliant wall, the plate deflection affects the near-wall turbulence. The compliant wall deflection into the buffer layer breaks the near-wall streaks and the associated quasi-streamwise vortices, and induces more spanwise coherence (Rosti and Brandt, 2017).

In this paper, we develop a formulation to obtain the wall-normal distribution of intensity and relative phase of the fluid sources responsible for the plate excitation. Previous research works do not yield such quantitative information of the fluid sources. The main idea is to express the plate averaged displacement PSD as a double wall-normal integral of the ‘net displacement source’ cross-spectral density (CSD) $\Gamma^a(r, s, \omega)$ across the height of the channel. The analysis framework combines the volumetric DNS data, Green’s function solution of the pressure fluctuation and modal superposition, and builds on the previous work of Anantharamu and Mahesh (2019). We then apply the framework to explain the one-way coupled FSI simulation results of an elastic plate in turbulent channel flow at $Re_\tau = 180$ and 400. The fluid and solid simulations make use of finite volume DNS and time-domain FEM, respectively. Further, the decorrelated fluid sources that contribute the most to plate response are obtained using spectral Proper Orthogonal Decomposition (POD) of the net displacement source CSD.

The organization of the paper is as follows: Section 2 discusses the validation of the in-house FEM solid solver - MPCUGLES-SOLID. In section 3, we describe the computational domain, mesh resolution, and the FSI simulation details. Section 4 discusses the novel one-way coupling analysis framework. In section 5.1, we discuss the obtained one-way coupled FSI results. Section 5.2 discusses the spectral features of the net displacement source CSD and in section 5.3, we identify the decorrelated features of the fluid source using spectral POD. Finally, we summarize the results in section 6.

Note that x , y and z denote the streamwise, spanwise and wall-normal coordinates, respectively. Superscripts/subscripts f and s denote fluid and solid quantities, respectively.

2. Validation of the in-house FEM solid solver - MPCUGLES-SOLID

The in-house FEM solid solver - MPCUGLES-SOLID - is a time-domain solver that uses the continuous Galerkin method to solve the dynamic linear elasticity equations. We validate the solver’s ability to simulate random vibration problems by simulating the Han, Bernhard and Mongeau (1999) experiment using synthetically generated loads. Han et al. (1999) measured the response of a rectangular steel plate excited by a turbulent boundary layer at $Re_\tau \approx 2000$. Table 1 shows the dimensions of the plate and the boundary layer properties in the experiment. Note that the plate lies in the $x - z$ plane. We first generate the wall-pressure fluctuations synthetically using a Fourier series methodology based on the experimental conditions. Then, we compare the obtained time-domain response of the plate from the solver to the experiment. The generated fluctuations obey the Corcos (Corcos, 1964) CSD model and the Smolyakov-Tkachenko (Smol’Iakov and Tkachenko, 1991) PSD model.

Plate length (L_x^s)	0.47m
Plate width (L_z^s)	0.37m
Plate thickness (L_y^s)	$1.59 \times 10^{-3}m$
Displacement thickness	$2.4 \times 10^{-3}m$
Flow velocity	$44.7ms^{-1}$
Plate material	Steel

Table 1

Plate properties, dimensions and experimental conditions of the Han et al. (1999) experiment used to validate the solver.

We express the wall-pressure fluctuation ($p_w(x, z, t)$) as the Fourier series,

$$p_w(x, z, t) = \sum_{l=-N_x^f/2}^{N_x^f/2-1} \sum_{m=-N_z^f/2}^{N_z^f/2-1} \sum_{n=-N_t^f/2}^{N_t^f/2-1} \hat{p}_{l,m,n} e^{i(k_l x + k_m z + \omega_n t)},$$

$$\hat{p}_{l,m,n} = \left(\frac{2\pi}{L_x^f} \frac{2\pi}{L_z^f} \frac{2\pi}{T^f} \phi_{pp}(k_l, k_m, \omega_n) \right)^{1/2} e^{i\theta},$$

$$k_l = \frac{2\pi l}{L_x^f}; k_m = \frac{2\pi m}{L_z^f}; \omega_n = \frac{2\pi n}{T^f}.$$
(2)

Here, L_x^f and L_z^f are the length and width of the domain used to generate the fluctuations, respectively, T^f is the timespan of the generated fluctuations, θ is a uniformly distributed random number between 0 and 2π , N_x^f , N_z^f , and N_t^f are the number of terms used to truncate the Fourier series in each dimension, and $\phi_{pp}(k_l, k_m, \omega_n)$ is the wavenumber-frequency spectrum of the wall-pressure fluctuations. The length and width of the domain used to generate the load is ten times the size of the plate, i.e., $L_x^f = 10L_x^s$ and $L_z^f = 10L_z^s$. In this way, we include the contribution of the low wavenumber wall-pressure fluctuations ($|\vec{k}| < |\vec{k}_j|$) to plate excitation. The timespan of the generated wall-pressure fluctuations is 840 times the period of the first mode of vibration of the plate, i.e., $T^f = 840(2\pi/\omega_1)$, where ω_1 is the first natural frequency of the plate. Hence, we allow sufficient time for the transient response to decay. For the wavenumber- frequency spectrum ($\phi_{pp}(k_l, k_m, \omega_n)$) in the above equation, we set

$$\phi_{pp}(k_x, k_z, \omega) = \phi_{pp}(\omega) \frac{\alpha_x}{\pi} \frac{\alpha_z}{\pi} \left(\frac{\omega}{U_c} \right)^2 \left(\left(\frac{\alpha_x \omega}{U_c} \right)^2 + \left(\frac{\omega}{U_c} + k_x \right)^2 \right)^{-1} \left(\left(\frac{\alpha_x \omega}{U_c} \right)^2 + k_z^2 \right)^{-1},$$

$$\frac{\phi_{pp}(\omega)}{\tau_w^2 \delta^* / U_\infty} = \frac{1}{2} \frac{5.1}{1 + 0.44 \left(\frac{|\omega| \delta^*}{U_\infty} \right)^{7/3}},$$
(3)

where we use the experimental conditions given in table for δ^* and U_∞ . For U_c , we use a constant value of $0.89U_\infty$, and for τ_w , we use the relation, $\tau_w \approx 0.0225 \rho_f U_\infty^2 Re_\delta^{-1/4}$ (equation 21.5 in Schlichting (1979)), where $Re_\delta = \frac{U_\infty \delta^*}{\nu}$. We generate the Fourier coefficients ($\hat{p}_{l,m,n}$) only in the right half-plane in wavenumber space. To set the coefficients in the left-half plane, we use the fact that the Fourier coefficients of a real function are conjugate symmetric, i.e., $\hat{p}_{-l,-m,-n} = \hat{p}_{l,m,n}^*$. This ensures that the generated wall-pressure fluctuations are real. Rogallo (1981) used a similar technique to generate the initial velocity field in the isotropic turbulence decay simulations. Maxit (2016) used a similar approach to generate multiple realizations of the Fourier transform of the pressure fluctuation for frequency-domain response. Here, we generate only one time-domain realization of the space-time wall-pressure fluctuations. Note that this approach applies to any spatially homogenous wall-pressure cross spectral density model. Since this a time-domain approach, even the response of nonlinear structures can be obtained from the generated synthetic wall-pressure fluctuations.

We use a Cartesian mesh to discretize the solid domain. The number of elements in the streamwise, spanwise and thickness directions is 32, 32, and 1, respectively. We use hexahedral elements of polynomials of degree 2. The

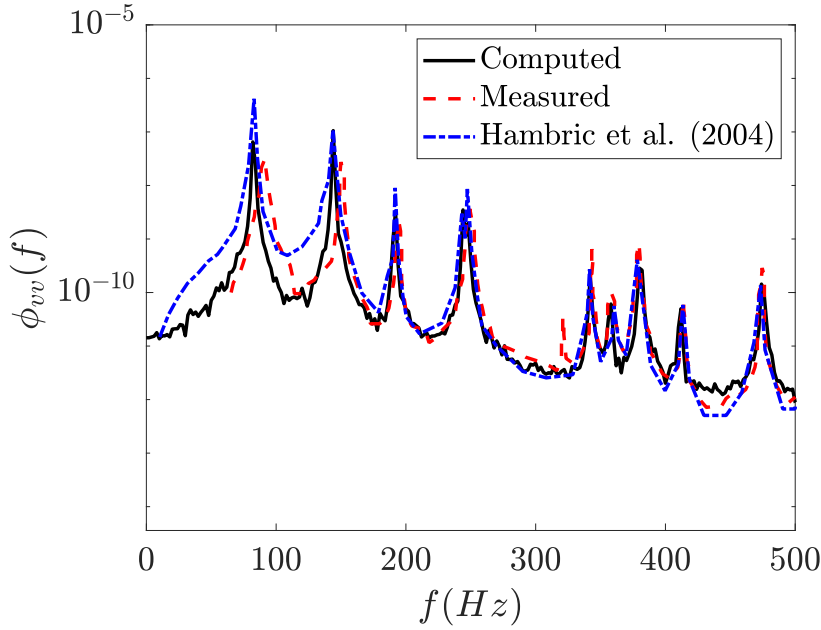


Figure 1: Comparison of the wall-normal velocity spectra at a point $(0.15m, 0.12m)$ on the plate for the validation case.

number of frequencies (N_t^f) and wavenumbers ($N_x^f = N_z^f$) used to generate the load is 10000 and 320, respectively. We make use of a parallel implementation to generate the synthetic wall-pressure fluctuations that consists of ≈ 1 billion terms. To efficiently compute the exact surface forces from the generated wall-pressure fluctuations, we make use of L^2 orthogonal projection (Powell, 1981) of the Fourier series (equation 2) onto polynomials of degree 2 within each boundary surface element. For details of force computation, we refer the reader to appendix A. The timestep of the solid simulation is 5×10^{-5} s, and the total simulation time is 10 s. We discard the first 5 s since they contain the transient response. We use the following 5 s to compute the statistics.

Figure 1 shows the comparison of the computed velocity PSD at a point $(0.15m, 0.12m)$ on the top surface of the plate to the measurement of Han et al. (1999). The PSD agrees well with the experiment. In the figure, we also compare our time-domain results to the frequency domain results of Hambric et al. (2004). Hambric et al. (2004) used the modified Corcos wall-pressure wavenumber frequency spectrum (Hwang and Maidanik, 1990) to compute the plate response. Even though the spectral level of the standard Corcos (Corcos, 1964) (that we use) is higher compared to the modified Corcos in the low wavenumber range, our simulation results are closer to the experiment than Hambric et al. (2004). Also, the low-frequency spectral levels shown in figure 1 are smaller than Hambric et al. (2004) when one might expect the opposite. We believe this is due to the finite domain size used to generate the load. The finite domain sets a lower bound on the wavenumbers contributing to the excitation.

3. FSI simulation details

3.1. Computational domain

Figure 2 shows a schematic of the fluid and solid computational domain and table 2 shows the domain extents. The fluid computational domain is a Cartesian box of size $L_x^f \times L_y^f \times L_z^f$. We choose $L_x^f = 6\pi\delta$, $L_y^f = 2\delta$ and $L_z^f = 2\pi\delta$, where δ is the half channel height. Long streamwise and spanwise domains include the contribution of large scale structures to pressure fluctuations. The solid computational domain is a rectangular plate clamped on all sides placed at the bottom wall of the channel. The plate is flush with the bottom wall and centered. The length (L_x^s), width (L_y^s), and thickness (L_z^s) of the plate is $6\pi\delta/5$, $2\pi\delta/5$ and 0.004δ , respectively. The smaller dimension of the plate ensures that the pressure fluctuations with wavelengths larger than the plate dimensions are present in the computational box. Thus, we include the low wavenumber ($k_1 \ll k_{m,j}$) wall-pressure fluctuation contribution to plate excitation.

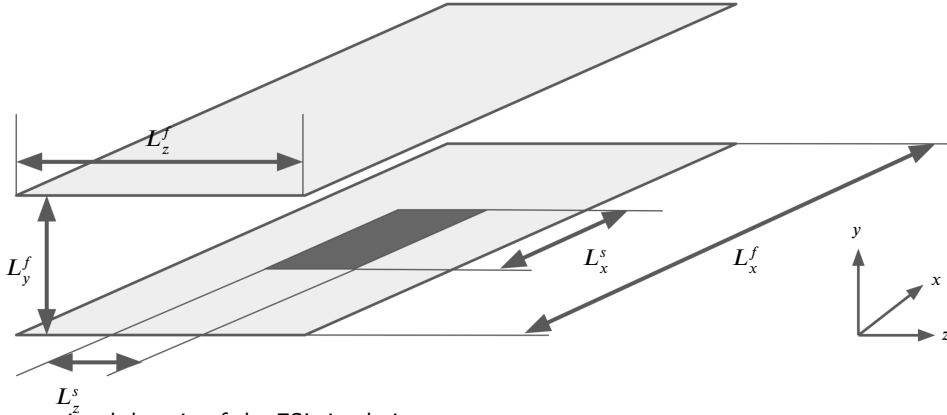


Figure 2: Computational domain of the FSI simulation.

$$\begin{array}{cc} L_x^f \times L_y^f \times L_z^f & L_x^s \times L_y^s \times L_z^s \\ 6\pi\delta \times 2\delta \times 2\pi\delta & (6\pi/5)\delta \times 0.004\delta \times (2\pi/5)\delta \end{array}$$

Table 2

Fluid and solid domain extents.

Re_τ	$N_x^f \times N_y^f \times N_z^f$	$N_x^s \times N_y^s \times N_z^s$	Δx^+	Δz^+	Δy_w^{f+}	Δy_c^{f+}
180	$720 \times 176 \times 330$	$144 \times 1 \times 66$	4.7	3.4	0.27	4.4
400	$1388 \times 288 \times 660$	$288 \times 1 \times 132$	5.4	3.8	0.37	5.9

Table 3

Fluid and solid mesh sizes and resolution of the FSI simulation. Note that the fluid and solid meshes match at the interface.

3.2. Fluid DNS

We solve the incompressible Navier-Stokes equations in the fluid domain using the collocated finite volume method of Mahesh, Constantinescu and Moin (2004) in a frame of reference moving with the bulk velocity of the fluid as done by Bernardini, Pirozzoli, Quadrio and Orlandi (2013). This lead to better prediction of the high frequency component of the pressure spectra. The walls in the channel are assumed to be rigid in the fluid calculation. For time integration, we use the Crank-Nicholson scheme. Overall, the method is second order accurate in space and time, and non-dissipative. The algorithm conserves kinetic energy discretely. This ensures stability of the algorithm at high Reynolds numbers without adding numerical dissipation. We perform the DNS using the in-house flow solver - MPCUGLES.

The fluid mesh is cartesian. The mesh is uniform in the streamwise and spanwise directions. In the wall-normal direction, we use a non-uniform hyperbolic tangent spacing to cluster control volumes near the wall. Table 3 shows the fluid mesh sizes and resolutions for both Re_τ . The streamwise spacing (Δx^+), spanwise spacing (Δz^+), the wall-normal spacing near the wall (Δy_w^{f+}) and channel centerline (Δy_c^{f+}) is fine enough to resolve the fine-scale features of wall turbulence. The timestep of the fluid simulation is $5 \times 10^{-4} \delta / u_\tau$ for both Re_τ . The velocity (U_b / u_τ) of the moving reference frame is 15.8 and 17.8 in the streamwise direction for $Re_\tau = 180$ and 400, respectively. We employ a slip velocity boundary condition (equal to $-U_b / u_\tau$) at the top and bottom wall. For pressure, we use a zero Neumann boundary condition at the top and bottom wall. In the streamwise and spanwise directions, we use periodic boundary conditions for both velocity and pressure. For validation of the fluid DNS, we refer the reader to Anantharamu and Mahesh (2019).

Young's modulus ($E/(\rho_f u_\tau^2)$)	6.88×10^9
Poisson ratio (ν_s)	0.4
Solid density (ρ_s/ρ_f)	1.17×10^3

Table 4

Non-dimensional properties of the plate.

3.3. Solid simulation

We solve the three-dimensional dynamic linear elasticity equations in the solid domain with the continuous Galerkin Finite Element Method (abbreviated as just FEM). We perform the solid simulation using the validated in-house solid solver - MPCUGLES-SOLID. We use second-order polynomials in each element to represent the solution and trapezoidal rule for the time integration of the equations. We precondition the matrix problem using the scaled thickness preconditioner developed by Klöppel, Gee and Wall (2011) with the optimal scaling $\frac{L_x^s/N_x^s + L_z^s/N_z^s}{2L_y^s}$. The preconditioner reduced the simulation time by a factor of 3.

We non-dimensionalize the structural equations with the half-channel height (δ), fluid density (ρ_f), and friction velocity (u_τ). The non-dimensional properties of the plate are shown in table 4. We use a mass proportional Rayleigh damping of 2.25. The structural loss factor with the chosen mass proportional damping is 0.05 at the first natural frequency. The solid simulation timestep is the same as the fluid DNS.

The solid mesh is Cartesian and composed of 27-node hexahedral elements. Table 3 gives the dimensions of the mesh. Since the plate is of high aspect ratio, we only use one element in the thickness direction. Further, the fluid and solid meshes match at the interface. Thus, no special load transfer strategy is required. We set the displacement of the nodes on all four sides of the plate to zero and apply the rigid wall DNS wall-pressure fluctuations onto the top surface of the plate.

The fluid DNS is first run until it reaches a statistically stationary state. Then, the one-way coupled FSI simulation is run for a total time of $16\delta/u_\tau$ units. We discard the first $8\delta/u_\tau$ time units of the solid response as it contains the transient response of the solid and use the remaining $8\delta/u_\tau$ time units to compute the statistics of the plate response.

4. Analysis framework

4.1. Theory

The goal is to express the plate averaged displacement PSD as a double integral over all the wall-parallel plane pairs. To accomplish this, we first express the bottom wall displacement $d(x, -\delta, z, t)$ as a wall-normal integral,

$$d(x, -\delta, z, t) = \int_{-\delta}^{+\delta} f_d(x, y, z, t) dy. \quad (4)$$

Here, $f_d(x, y, z, t)$ is called the ‘net displacement source’ (exact form is derived later). It gives the contribution of each wall-parallel plane to the surface displacement of the plate. We define the plate averaged displacement PSD $\phi_{dd}^a(\omega)$ as

$$\begin{aligned} \phi_{dd}^a(\omega) &= \frac{1}{A_p} \iint_{\Gamma_{fs}} \phi_{dd}(x, -\delta, z, \omega) dx dz, \\ \phi_{dd}(x, -\delta, z, \omega) &= \frac{1}{2\pi} \int_{-\infty}^{+\infty} d^*(x, -\delta, z, t) d(x, -\delta, z, t + \tau) e^{-i\omega\tau} d\tau, \end{aligned} \quad (5)$$

where $\phi_{dd}(x, -\delta, z, \omega)$ is the displacement PSD at a point $(x, -\delta, z)$ on the surface of the plate, and A_p is the area of the plate and Γ_{fs} is the plate surface. We can then relate the plate averaged displacement PSD $\phi_{dd}^a(\omega)$ to the net displacement source $f_d(x, y, z, t)$ using equations 4 and 5 as

$$\begin{aligned} \phi_{dd}^a(\omega) &= \iint_{-\delta}^{+\delta} \Gamma^a(r, s, \omega) dr ds, \\ \Gamma^a(r, s, \omega) &= \frac{1}{A_p} \int_{\Gamma_{fs}} \left(\frac{1}{2\pi} \int_{-\infty}^{+\infty} \langle f_d^*(x, r, z, t) f_d(x, s, z, t + \tau) \rangle e^{-i\omega\tau} d\tau \right) dx dz, \end{aligned} \quad (6)$$

where $\Gamma^a(r, s, \omega)$ is the plate averaged CSD of $f_d(x, y, z, t)$. The function $\Gamma^a(r, s, \omega)$ yields the contribution of each wall-parallel plane pair to the PSD $\phi_{dd}^a(\omega)$ for different frequencies.

We obtain $f_d(x, y, z, t)$ as follows. Express $d(x, -\delta, z, t)$ in the modal basis as

$$d(x, -\delta, z, t) = \sum_{j=1}^{\infty} d_j(t) \varphi_j(x, -\delta, z), \quad (7)$$

where, $\varphi_j(x, -\delta, z)$ is the wall-normal component of the j^{th} mode shape on the top surface of the plate, and $d_j(t)$ is the component of the solution along the j^{th} mode shape. Assuming zero initial displacement and velocity of the plate, we write the solution for $d_j(t)$ using the Duhamel integral (Bathe, 2006) as

$$d_j(t) = \frac{1}{\bar{\omega}_j} \int_0^t f_j(\tau) e^{-\xi_j \omega_j(t-\tau)} \sin(\bar{\omega}_j(t-\tau)) d\tau, \quad (8)$$

where $\bar{\omega}_j = \omega_j \sqrt{1 - \xi_j^2}$, and $f_j(t)$ is the modal force of the j^{th} mode shape of the plate given by

$$f_j(t) = - \iint_{\Gamma_{fs}} p(x, -\delta, z, t) \varphi_j(x, -\delta, z) dx dz. \quad (9)$$

To account for only the steady state response, we use a large value for t in equation 5. For large enough t , the initial transient contribution to the response of the plate decays to small values, thus leaving only the steady state contribution. To express $p(x, -\delta, z, t)$ as a wall-normal integral, we use the pressure fluctuation Poisson equation,

$$-\nabla^2 p = f = \rho_f \left(2 \frac{\partial U_i^f}{\partial x_j} \frac{\partial u_j^{f'}}{\partial x_i} + \frac{\partial^2}{\partial x_i \partial x_j} \left(u_i^{f'} u_j^{f'} - \overline{u_i^{f'} u_j^{f'}} \right) \right), \quad (10)$$

where U_i^f and $u_i^{f'}$ are the mean and fluctuating fluid velocities, respectively. Neglecting the Stokes contribution, we use a zero Neumann boundary condition at the top and bottom walls for the pressure fluctuations. This is reasonable as the Stokes component of wall-pressure fluctuations is small at high Reynolds number (Hoyas and Jiménez, 2006). To obtain a unique solution, we set the average of the pressure fluctuations at the top and bottom wall to zero at all times. The solution to the pressure fluctuations $p(x, -\delta, z, t)$ at the bottom wall is then,

$$\begin{aligned} p(x, -\delta, z, t) &= \int_{-\delta}^{+\delta} f_G(x, y, z, t) dy, \\ f_G(x, y, z, t) &= \iint_{-\infty}^{+\infty} G(-\delta, y, k) \hat{f}(k_1, y, k_3, t) e^{i(k_1 x + k_3 z)} dk_1 dk_3, \\ k &= \sqrt{k_1^2 + k_3^2}, \\ G(r, s, k) &= \begin{cases} \frac{\cosh(k(s-\delta)) \cosh(k(r+\delta))}{2k \sinh(k\delta) \cosh(k\delta)}, & r \leq s, \\ \frac{\cosh(k(s+\delta)) \cosh(k(r-\delta))}{2k \sinh(k\delta) \cosh(k\delta)}, & r > s, \end{cases} \end{aligned} \quad (11)$$

where $f_G(x, y, z, t)$ is termed the ‘net source’ function (Anantharamu and Mahesh, 2019), $G(-\delta, y, k)$ is the Green’s function, and $\hat{f}(k_1, y, k_3, t)$ is the multidimensional Fourier transform of the source terms $f(x, y, z, t)$ defined as

$$\hat{f}(k_1, y, k_3, t) = \frac{1}{(2\pi)^2} \iint_{-\infty}^{+\infty} f(x, y, z, t) e^{-i(k_1 x + k_3 z)} dx dz. \quad (12)$$

We call $f_G(x, y, z, t)$ the ‘net source’ function because it includes contributions from all wavenumbers and the Green’s function. Combining equations 7, 8, 9 and 11, we obtain the required expression for the net displacement source

$f_d(x, y, z, t)$ as

$$f_d(x, y, z, t) = \sum_{j=1}^{\infty} \frac{1}{\bar{\omega}_j} \left(\int_0^t \left(\iint_{\Gamma_{fs}} f_G(x, y, z, t) \varphi_j(x, -\delta, z) dx dz \right) e^{-\xi_j \omega_j(t-\tau)} \sin(\bar{\omega}_j(t-\tau)) d\tau \right) \varphi_j(x, -\delta, z) \quad (13)$$

To obtain the contribution from the cross-correlation of the fluid sources with a particular plane $y = r$ to the plate averaged response PSD, we integrate $\Gamma^a(r, s, \omega)$ along s to obtain $\Psi^a(r, \omega)$,

$$\Psi^a(r, \omega) = \int_{-\delta}^{+\delta} \Gamma^a(r, s, \omega) ds. \quad (14)$$

It can be shown that $\Psi_a(r, \omega)$ is the plate averaged wall displacement-net displacement source CSD,

$$\Psi^a(r, \omega) = \frac{1}{A_p} \int_{\Gamma_{fs}} \left(\frac{1}{2\pi} \int_{-\infty}^{+\infty} \langle f_d^*(x, r, z, t) d(x, -\delta, z, t + \tau) \rangle e^{-i\omega\tau} d\tau \right) dx dz. \quad (15)$$

Further, the plate averaged wall displacement-net displacement source CSD relates to the plate averaged displacement PSD $\phi_{dd}^a(\omega)$ as

$$\phi_{dd}^a(\omega) = \int_{-\delta}^{+\delta} \Psi^a(r, \omega) dr = \int_{-\delta}^{+\delta} \text{Re}(\Psi^a(r, \omega)) dr, \quad (16)$$

where $\text{Re}(\cdot)$ is the real part of \cdot .

We relate the plate averaged net displacement source CSD $\Gamma_a(r, s, \omega)$ to the four-dimensional CSD of the pressure fluctuation source terms $\varphi_{ff}(r, s, k_1, k_3, \omega)$ as follows. The four-dimensional CSD $\varphi_{ff}(r, s, k_1, k_3, \omega)$ is defined as

$$\varphi_{ff}(r, s, k_1, k_3, \omega) = \frac{1}{(2\pi)^3} \iiint_{-\infty}^{+\infty} \langle f^*(x, z, r, t) f(x + \xi_1, z + \xi_3, s, t + \tau) \rangle e^{-i(k_1 \xi_1 + k_3 \xi_3 + \omega\tau)} d\xi_1 d\xi_3 d\tau. \quad (17)$$

Neglecting the transient response of the plate, the modal displacement PSD $\phi_{d_j d_j}(\omega)$ relates to the modal force PSD $\phi_{f_j f_j}(\omega)$ as

$$\begin{aligned} \phi_{d_j d_j}(\omega) &= |H_j(\omega)|^2 \phi_{f_j f_j}(\omega), \\ H_j(\omega) &= \frac{1}{(\omega_j^2 - \omega^2) + i2\xi_j \omega_j \omega}, \end{aligned} \quad (18)$$

where $|H_j(\omega)|^2$ is the gain in the response of the j^{th} mode. Further, the modal force $\phi_{f_j f_j}(\omega)$ relates to the wall-pressure wavenumber frequency spectrum $\phi_{pp}(k_1, k_3, \omega)$ as

$$\phi_{f_j f_j}(\omega) = \iint_{-\infty}^{+\infty} \phi_{pp}(k_1, k_3, \omega) |S_j(k_1, k_3)|^2 dk_1 dk_3. \quad (19)$$

Relating $\phi_{pp}(k_1, k_3, \omega)$ to the four-dimensional CSD $\varphi_{ff}(r, s, k_1, k_3, \omega)$ using the Green's function, we obtain

$$\begin{aligned} \phi_{f_j f_j}(\omega) &= \iint_{-\delta}^{+\delta} \iint_{-\infty}^{+\infty} G^*(-\delta, r, k) G(-\delta, s, k) \varphi_{ff}(r, s, k_1, k_3, \omega) \\ &\quad |S_j(k_1, k_3)|^2 dk_1 dk_3 dr ds, \end{aligned} \quad (20)$$

where $S_j(k_1, k_3) = \iint_{\Gamma_{fs}} \varphi_j(x, 0, z) e^{i(k_1 x + k_3 z)} dx dz$ is the Fourier transform of the mode shape, and $|S_j(k_1, k_3)|^2$ is the ‘modal shape function’ (Hwang and Maidanik, 1990). Next, we relate the plate averaged displacement PSD $\phi_{dd}^a(\omega)$ to the modal displacement PSD $\phi_{d_j d_j}(\omega)$ as

$$\begin{aligned} \phi_{dd}^a(\omega) &= \frac{1}{A_p} \iint_{\Gamma_{fs}} \phi_{dd}(x, -\delta, z) dx dz, \\ &= \frac{1}{A_p} \iint_{\Gamma_{fs}} \sum_{i=1}^{\infty} \sum_{j=1}^{\infty} \phi_{d_i d_j}(\omega) \varphi_i(x, -\delta, z) \varphi_j(x, -\delta, z) dx dz, \\ &\approx \frac{1}{\rho_s L_y^s A_p} \sum_{j=1}^{\infty} \phi_{d_j d_j}(\omega) \left(\because \iint_{\Gamma_{fs}} \varphi_i(x, -\delta, z) \varphi_j(x, -\delta, z) dx dz \approx \frac{1}{\rho L_y^s} \delta_{ij} \right) \end{aligned} \quad (21)$$

Thus, combining equations 18, 20, and 21, we obtain the required expression

$$\begin{aligned} \Gamma^a(r, s, \omega) &\approx \frac{1}{\rho L_y^s A_p} \iint_{-\infty}^{+\infty} G^*(-\delta, r, k) G(-\delta, s, k) \varphi_{ff}(r, s, k_1, k_3, \omega) \\ &\quad \left(\sum_{j=1}^{\infty} |S_j(k_1, k_3)|^2 |H_j(\omega)|^2 \right) dk_1 dk_3. \end{aligned} \quad (22)$$

We investigate the structure of the decorrelated contribution from wall-parallel planes by performing spectral POD of the CSD $\Gamma^a(r, s, \omega)$. We use the following inner product to define the orthonormal relation between the eigenfunctions $\bar{\Phi}_i$ and $\bar{\Phi}_j$ of $\Gamma^a(r, s, \omega)$,

$$\int_{-\delta}^{+\delta} \left(\left(-(1-\beta) \frac{\partial^2}{\partial y^2} + \beta \right) \bar{\Phi}_i \right) \bar{\Phi}_j^* dy = \delta_{ij}, \quad (23)$$

where β is a real number satisfying $0 < \beta \leq 1$ and δ_{ij} is the Kroenecker delta. Further, the eigenfunctions $\bar{\Phi}_i(r, \omega)$ are assumed to satisfy the zero-Neumann boundary conditions at the wall $r = -\delta$ and $r = +\delta$. Following Anantharamu and Mahesh (2019), we call the above inner product as the Poisson inner product because the symmetric positive definite kernel $\left(-(1-\beta) \frac{\partial^2}{\partial y^2} + \beta \right)$ relates to the Poisson equation. The spectral POD of $\Gamma^a(r, s, \omega)$ is then

$$\Gamma^a(r, s, \omega) = \sum_{j=1}^{\infty} \lambda_j(\omega) \Phi_j(r, \omega) \Phi_j^*(s, \omega), \quad (24)$$

where $\{\Phi_j, \lambda_j\}_{j=1}^{\infty}$ is the set of spectral POD modes and eigenvalues. The spectral POD mode Φ_j relates to the eigenfunction $\bar{\Phi}_j$ of $\Gamma^a(r, s, \omega)$ through the relation $\Phi_j = \left(-(1-\beta) \frac{\partial^2}{\partial y^2} + \beta \right) \bar{\Phi}_j$. The associated eigenvalue problem for $\bar{\Phi}_j$ and λ_j is

$$\int_{-\delta}^{+\delta} \Gamma^a(r, s, \omega) \bar{\Phi}_j(s, \omega) ds = \lambda_j(\omega) \left(\left(-(1-\beta) \frac{\partial^2}{\partial y^2} + \beta \right) \bar{\Phi}_j \right) (r, \omega). \quad (25)$$

Further, the functions $\{\Phi_j\}_{j=1}^{\infty}$ and $\{\bar{\Phi}_j\}_{j=1}^{\infty}$ satisfy the orthonormality relation

$$\int_{-\delta}^{+\delta} \Phi_i(y, \omega) \bar{\Phi}_j^*(y, \omega) dy = \delta_{ij}. \quad (26)$$

The sum of the obtained spectral POD eigenvalues gives ranked contribution from each spectral POD mode to the following double integral,

$$\iint_{-\delta}^{+\delta} \frac{G\left(r, s, \frac{\beta}{1-\beta}\right)}{1-\beta} \Gamma^a(r, s, \omega) dr ds = \sum_{j=1}^{\infty} \lambda_j(\omega) \quad (27)$$

where $G(r, s, \beta/(1-\beta))$ is the Green's function given by equation 11. For small values of β , the function $G(r, s, \beta/(1-\beta))$ becomes flatter and approaches a constant in r and s , and the left hand side $\iint_{-\delta}^{+\delta} \frac{G(r, s, \frac{\beta}{1-\beta})}{1-\beta} \Gamma^a(r, s, \omega) dr ds$ becomes a good proxy for the plate averaged displacement PSD $\phi_{dd}^a(\omega) = \iint_{-\delta}^{+\delta} \Gamma^a(r, s, \omega) dr ds$. Therefore, the obtained spectral POD modes isolate the dominant contributors to plate averaged displacement PSD. For more details about the effectiveness of the Poisson inner product, we refer the reader to Anantharamu and Mahesh (2019).

To obtain the contribution of each spectral POD mode to the plate averaged displacement PSD, we doubly integrate equation 24 to obtain

$$\begin{aligned} \phi_{dd}^a(\omega) &= \sum_{j=1}^{\infty} \gamma_j(\omega), \\ \gamma_j(\omega) &= \lambda_j(\omega) \left| \int_{-\delta}^{+\delta} \Phi_j(y, \omega) dy \right|^2; j = 1, \dots, \infty, \end{aligned} \quad (28)$$

where $\gamma_j(\omega)$ is the contribution of j^{th} mode to PSD at frequency ω . Further, we can show that

$$\left| \int_{-\delta}^{+\delta} \Phi_j(y, \omega) dy \right| = \int_{-\delta}^{+\delta} |\Phi_j(y, \omega)| \cos(\angle \Phi_j(y, \omega) - \angle \Phi_j^n(\omega)) dy, \quad (29)$$

where $\angle \cdot$ is the argument of \cdot , and $\angle \Phi_j^n(\omega)$ is the argument of the integral $\int_{-\delta}^{+\delta} \Phi_j(y, \omega) dy$. Using equation 29 in equation 28, we obtain

$$\gamma_j(\omega) = \lambda_j(\omega) \left(\int_{-\delta}^{+\delta} |\Phi_j(y, \omega)| \cos(\angle \Phi_j(y, \omega) - \angle \Phi_j^n(\omega)) dy \right)^2; j = 1, \dots, \infty. \quad (30)$$

From the above equation, we observe that the eigenvalue, and both magnitude and phase of the spectral POD mode all play a role in determining its contribution to plate averaged displacement PSD. The contribution from different wall-normal locations can constructively or destructively interfere based on the phase of the spectral POD mode. Constructive interference occurs between the contribution from regions where the phase angle satisfies $|\angle \Phi_j(y, \omega) - \angle \Phi_j^n(\omega)| < \pi/2$. Further, the contribution from regions with the phase angle in the range $|\angle \Phi_j(y, \omega) - \angle \Phi_j^n(\omega)| < \pi/2$ destructively interfere with the regions where $\pi/2 < |\angle \Phi_j(y, \omega) - \angle \Phi_j^n(\omega)| < \pi$.

To obtain the contribution of each spectral POD mode to the integrated energy of the net displacement source, we set $s = r$ in equation 24 and integrate along r ,

$$\begin{aligned} \int_{-\delta}^{+\delta} \Gamma^a(r, r, \omega) dr &= \sum_{j=1}^{\infty} \bar{\lambda}_j(\omega); \\ \bar{\lambda}_j(\omega) &= \lambda_j(\omega) \int_{-\delta}^{+\delta} |\Phi_j(r, \omega)|^2 dr, \end{aligned} \quad (31)$$

where $\bar{\lambda}_j$ is the contribution of the j^{th} spectral POD mode to the integrated net displacement source PSD.

4.2. Implementation

To compute the net displacement source CSD Γ^a , we need to store the four-dimensional CSD φ_{ff} from the fluid DNS (equation 22). However, storing this function is prohibitively memory intensive. For the $Re_\tau = 400$ case, assuming 2000 frequencies, approximately 1000 TB is required to store the four-dimensional function. To circumvent this issue, we use a parallel, streaming methodology presented in Anantharamu and Mahesh (2019) with a small modification. Anantharamu and Mahesh (2019) presented the implementation to compute the CSD $\Gamma(r, s, \omega) = \iint_{-\infty}^{+\infty} G^*(-\delta, r, k) G(-\delta, s, k) \varphi_{ff}(r, s, k_1, k_3, \omega) dk_1 dk_3$. We modified their implementation to compute the CSD Γ^a given by equation 22 instead. We use the first six mode shapes of the plate to perform the summation in equation 22. The first six mode shapes are sufficient to analyze the fluid sources responsible for the first four peaks in the plate averaged displacement spectra.

Re_τ	$\left(\langle d^{+2} \rangle\right)^{1/2}$	$\left(\langle v^{+2} \rangle\right)^{1/2}$
180	1.81×10^{-2}	5.32×10^{-3}
400	5.32×10^{-2}	7.87×10^{-3}

Table 5

Plate averaged Root Mean Square (RMS) displacement and velocity of the plate.

We use a total time of $8\delta/u_\tau$ (16000 timesteps) to compute the net displacement source CSD Γ^a for both Re_τ . The sampling interval is same as timestep of the FSI simulation. We divide the temporal data into chunks of size $1\delta/u_\tau$ (2000 timesteps) and use 50% overlap between the chunks to increase statistical convergence. We use Hanning window to reduce spectral leakage.

5. Results and discussion

5.1. FSI simulation results

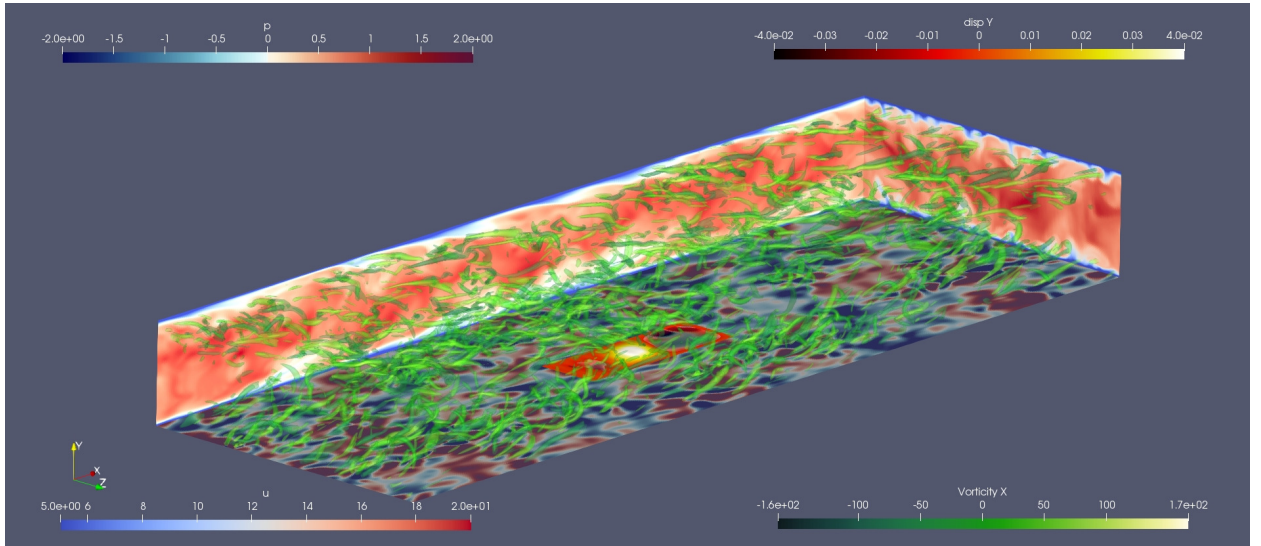


Figure 3: Instantaneous visualization of the FSI simulation at $Re_\tau = 180$.

Figure 3 shows an instantaneous visualization of the FSI simulation. The vertical and horizontal slices show the fluid streamwise velocity and wall-pressure fluctuations, respectively. The center patch denotes the deformed plate. The isosurfaces are of Q-criterion at non-dimensional values of 500 and 1000. The colored overlay on the isosurface denotes the streamwise component of vorticity. We use different colormaps for each quantity. The instantaneous field clearly shows the fine scale features of wall turbulence.

The plate averaged root mean square (RMS) wall-normal displacement and velocity for both Re_τ is given in table 5. Since, the RMS displacement and velocity is much lesser than 1 in viscous units, the one-way coupling is justified.

Figures 4a and b show the plate averaged wall-normal displacement spectra $\phi_{dd}^a(\omega)u_\tau/\delta^3$ (non-dimensionalized with δ and u_τ) for both Re_τ in outer and inner units, respectively. The time span of the temporal data used to compute the spectra is $8\delta/u_\tau$. We divide the temporal data into chunks of size $1\delta/u_\tau$ for averaging. To increase convergence and reduce spectral leakage, we use 50% overlap and Hanning window (Bendat and Piersol, 2011), respectively. The peaks in the spectra correspond to the natural frequencies ($\omega_j\delta/u_\tau$) of the plate. Further, these natural frequencies coincide in outer units for both Re_τ since the properties of the plate are the same in outer units for both the Reynolds numbers.

The low frequency ($\omega \ll \omega_1$) spectral levels overlap for both Re_τ . This is because i) the non-dimensional Young's modulus of the plate is the same for both Re_τ and ii) the low wavenumber and frequency component of the wall-pressure

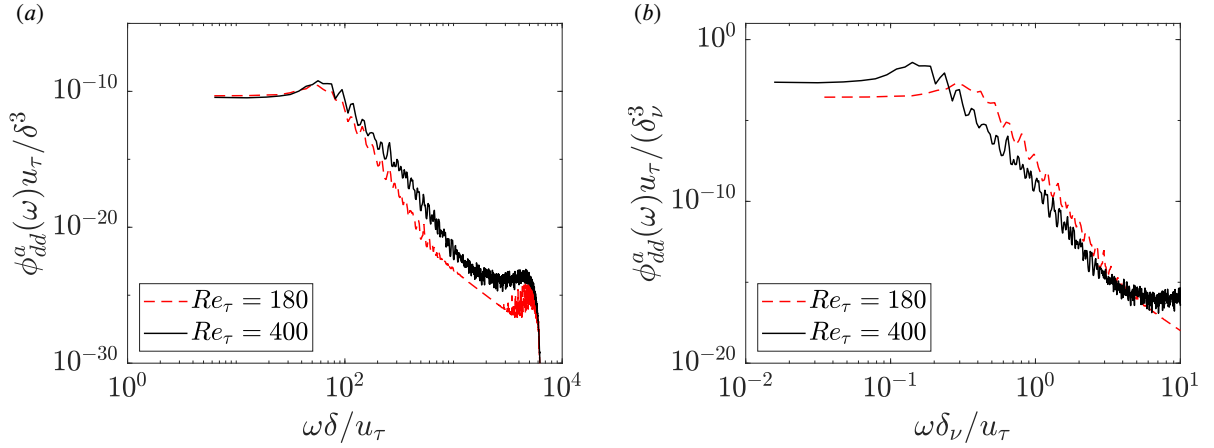


Figure 4: Plate averaged wall-normal displacement power spectra in a) outer units (normalized by δ and u_τ) and b) inner units (normalized by δ_v and u_τ).

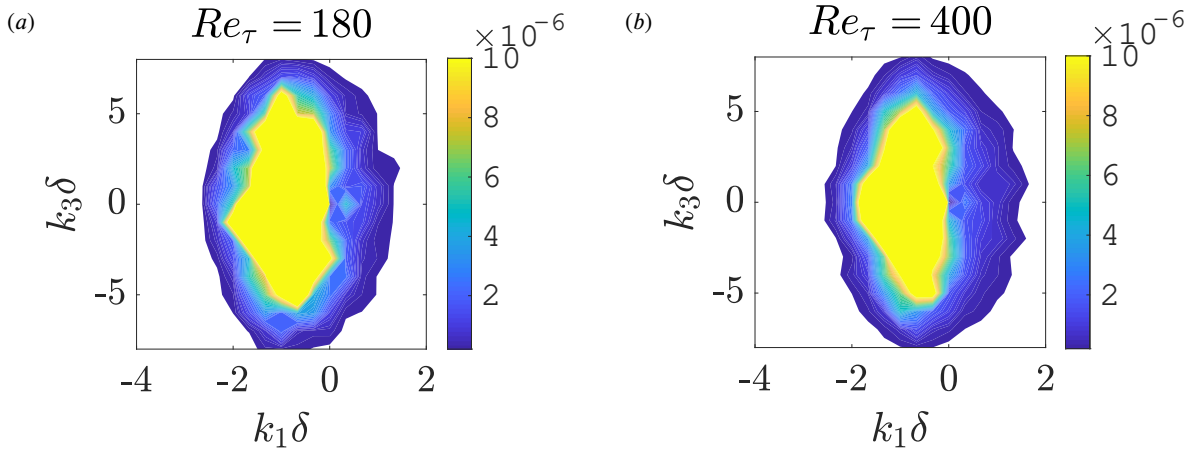


Figure 5: Product $|S_1(k_1, k_3)|^2 \phi_{pp}(k_1, k_3, \omega = 12.6u_\tau/\delta)$ for (a) $Re_\tau = 180$ and (b) $Re_\tau = 400$. Contours are 100 equally spaced values between 2×10^{-7} and 10^{-5} .

wavenumber-frequency spectrum is approximately the same in outer units for both Re_τ . We can understand this as follows.

Combining equations 18, 19, and 21, we have

$$\phi_{dd}^a(\omega) \approx \frac{1}{\rho_s L_y^s A_p} \sum_{j=1}^{\infty} |H_j(\omega)|^2 \iint_{-\infty}^{+\infty} \phi_{pp}(k_1, k_3, \omega) |S_j(k_1, k_3)|^2 dk_1 dk_3. \quad (32)$$

For frequencies $\omega \ll \omega_1$, we can approximate the average spectra using only the first mode as

$$\begin{aligned} \phi_{dd}^a(\omega) &\approx \frac{1}{\rho_s L_y^s A_p} |H_1(\omega)|^2 \iint_{-\infty}^{+\infty} \phi_{pp}(k_1, k_3, \omega) |S_1(k_1, k_3)|^2 dk_1 dk_3, \\ &\approx \frac{1}{\rho_s L_y^s A_p \omega_1^4} \iint_{-\infty}^{+\infty} \phi_{pp}(k_1, k_3, \omega) |S_1(k_1, k_3)|^2 dk_1 dk_3. \end{aligned} \quad (33)$$

Since, the first natural frequency (ω_1) is proportional to the longitudinal wave speed (c_l) of the plate, we have

$$c_l^4 \phi_{dd}^a(\omega) \propto \iint_{-\infty}^{+\infty} \phi_{pp}(k_1, k_3, \omega) |S_1(k_1, k_3)|^2 dk_1 dk_3. \quad (34)$$

Note that we have absorbed ρ_s , L_y^s , A_p into the proportionality constant. Non-dimensionalizing the above equation, we have

$$\left(\frac{c_l^4}{u_\tau^3}\right) \frac{\phi_{dd}^a(\omega)}{\delta^3} \approx C\left(\frac{\omega\delta}{u_\tau}, Re_\tau\right), \quad (35)$$

where C is some function of $\omega\delta/u_\tau$ and Re_τ only. We absorb the proportionality constant into C . Figures 5a and b show the product $|S_1(k_1, k_3)|^2 \phi_{pp}(k_1, k_3, \omega)$ for $Re_\tau = 180$ and 400 in outer units, respectively for a typical frequency $\omega\delta/u_\tau = 12.6 \ll \omega_1$. Overall, the contours are similar for both Re_τ . This similarity of contours occurs in the frequency range $\omega \ll \omega_1$. Thus, the dependency on Re_τ can be dropped, and we have

$$\left(\frac{c_l^4}{u_\tau^3}\right) \frac{\phi_{dd}^a(\omega)}{\delta^3} \approx C\left(\frac{\omega\delta}{u_\tau}\right). \quad (36)$$

Further, substituting for c_l in terms of the Young's modulus E , we have

$$\left(\frac{E}{\rho_s u_\tau^2}\right)^2 \frac{\phi_{dd}^a(\omega) u_\tau}{\delta^3} \approx C\left(\frac{\omega\delta}{u_\tau}\right). \quad (37)$$

Since, $\frac{E}{\rho_s u_\tau^2}$ is the same for both Re_τ , we have the required result,

$$\frac{\phi_{dd}^a(\omega) u_\tau}{\delta^3} \approx C\left(\frac{\omega\delta}{u_\tau}\right). \quad (38)$$

Figure 4b shows the plate averaged displacement PSD with inner scaling ($\delta_v = \nu_f/u_\tau$ and u_τ as length and velocity scale, respectively). The PSD at the two Re_τ do not overlap in the high-frequency region. This is because for identical natural frequencies in inner units, the corresponding modal wavenumbers do not match in inner units, i.e., if j and k are two mode indices such that

$$(\omega_j \delta_v / u_\tau)_{Re_\tau=180} = (\omega_k \delta_v / u_\tau)_{Re_\tau=400}, \quad (39)$$

then

$$(k_{m,j} \delta_v)_{Re_\tau=180} \neq (k_{m,k} \delta_v)_{Re_\tau=400}. \quad (40)$$

Therefore, the plate filters different wavenumbers from the wall-pressure wavenumber frequency spectra in viscous units leading to dissimilar high-frequency spectral levels.

A better overlap of high-frequency spectral levels is observed (shown in figure 6) if $E\delta^2/(\rho_f \nu_f^2)$ (velocity scale is ν_f/δ) is fixed for the two Reynolds numbers instead of $E/\rho_f u_\tau^2$ (velocity scale is u_τ). This is because for fixed $E\delta^2/(\rho_f \nu_f^2)$ and coinciding natural frequencies in inner units, the corresponding modal wavenumbers also coincide in inner units. We explain this as follows. Let j and k be the mode indices with coinciding natural frequencies in inner units for $Re_\tau = 180$ and 400, respectively, i.e.,

$$(\omega_j \delta_v / u_\tau)_{Re_\tau=180} \approx (\omega_k \delta_v / u_\tau)_{Re_\tau=400}. \quad (41)$$

We can show that for fixed $E\delta^2/(\rho_f \nu_f^2)$ and L_y^s/δ , we have

$$(k_{m,j} \delta)^2 \approx (k_{m,k} \delta)^2 \left(\frac{180}{400}\right)^2. \quad (42)$$

Further, non-dimensionalizing in viscous units, we obtain the desired relation,

$$(k_{m,j} \delta_v)_{Re_\tau=180} \approx (k_{m,k} \delta_v)_{Re_\tau=400} \quad (43)$$

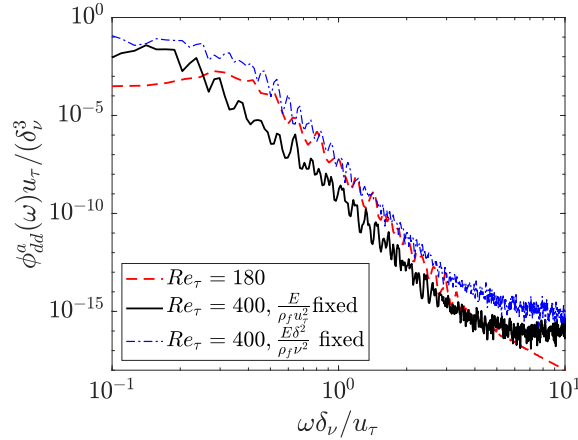


Figure 6: High frequency plate averaged displacement spectra comparison by fixing $E\delta^2/(\rho_f \nu^2)$ and $E/\rho_f u_\tau^2$ between the two Reynolds numbers.

5.2. Wall-normal distribution of fluid sources

Figures 7a and 7b show the contours of the computed plate averaged wall displacement-net displacement source CSD $\Psi_a(y^+, \omega\delta/u_\tau)$ (normalized by its integral) for $Re_\tau = 180$ and 400, respectively. y^+ is the distance from the wall. The three horizontal dashed red lines in both figures denote the first three peak frequencies ($\omega\delta/u_\tau = 50.2, 75.4$ and 94.25) of the plate averaged displacement PSD (figure 4a) and the red markers ‘x’ denote the wall-normal coordinate with maximum value of Ψ^a at the peak frequencies. From a visual inspection of the contours, we see that the location of maximum intensity and width of the fluid sources approximately depend on inner and outer units, respectively.

To investigate this further, we plot the CSD Ψ^a at the peak frequencies in figure 8 for both Re_τ . All three frequencies have a peak in buffer layer (around $y^+ \approx 10$). This implies that the correlation of the fluid sources with the buffer layer is a dominant contributor to the response of the plate. The CSD has reasonable values for $y/\delta \lesssim 0.75$. Thus, the correlation of fluid sources with wall-parallel planes within $y/\delta \approx 0.75$ have a sizeable contribution to the response. In other words, the width of the fluid sources contributing to the plate response depends on outer units and is approximately $y/\delta \approx 0.75$.

Further, Ψ^a is negative for small wall-normal regions around $y^+ \approx 40$ for $\omega\delta/u_\tau \approx 50.2$ (shown by white region). Thus, in a plate averaged sense, the plate displacement $\hat{d}(x, -\delta, z, \omega)$ and $\hat{f}_d(x, y, z, \omega)$ have phase difference θ satisfying $\pi/2 < |\theta| < \pi$. However, we do not observe such negative regions for $Re_\tau = 180$. This negative contribution comes from the coupling of the $Re_\tau = 400$ fluid sources with the lower mode shapes of the plate. More such negatively correlated regions close to the wall (shown by white regions) are seen in figure 7b. Further, the global peak for $Re_\tau = 400$ in figure 7b is at the coordinate $(y_p, \omega_p\delta/u_\tau) = (3, 44)$ (indicated by ‘+’ symbol) which is much closer to the wall than the $Re_\tau = 180$ peak location at $(y_p, \omega_p\delta/u_\tau) = (13, 50)$. These differences in the near wall region is because the natural frequencies and the modal wavenumbers are different in viscous units for the two Re_τ . But, the four-dimensional CSD $\phi_{ff}(r, s, k_1, k_3, \omega)$ can be expected to be similar in viscous units near to the wall for the two Reynolds numbers. Therefore, the plate inherently filters different wavenumbers and frequencies in viscous units from $\phi_{ff}(r, s, k_1, k_3, \omega)$ for the two Re_τ (equation 22), thus leading to different near-wall coupling with the fluid sources.

The Corcos form (Corcos, 1964) of the wall-pressure wavenumber frequency spectrum has an interesting implication on the associated one-way coupling. We show that for a Corcos type wavenumber frequency spectrum, the plate averaged displacement spectra and the wall-pressure PSD couple in a similar manner with the channel fluid sources upto a multiplicative constant. The Corcos type wavenumber-frequency spectrum $\phi_{pp}(k_1, k_3, \omega)$ takes the form,

$$\phi_{pp}(k_1, k_3, \omega) = \phi_{pp}(\omega) A\left(\frac{k_1 U_c}{\omega}\right) B\left(\frac{k_3 U_c}{\omega}\right), \quad (44)$$

where $A(k_1 U_c/\omega)$ and $B(k_3 U_c/\omega)$ are functions that describe the self-similar form of the streamwise and spanwise wavenumber dependence, respectively. The wall-pressure PSD $\phi_{pp}(\omega)$ can be expressed as the wall-normal integral

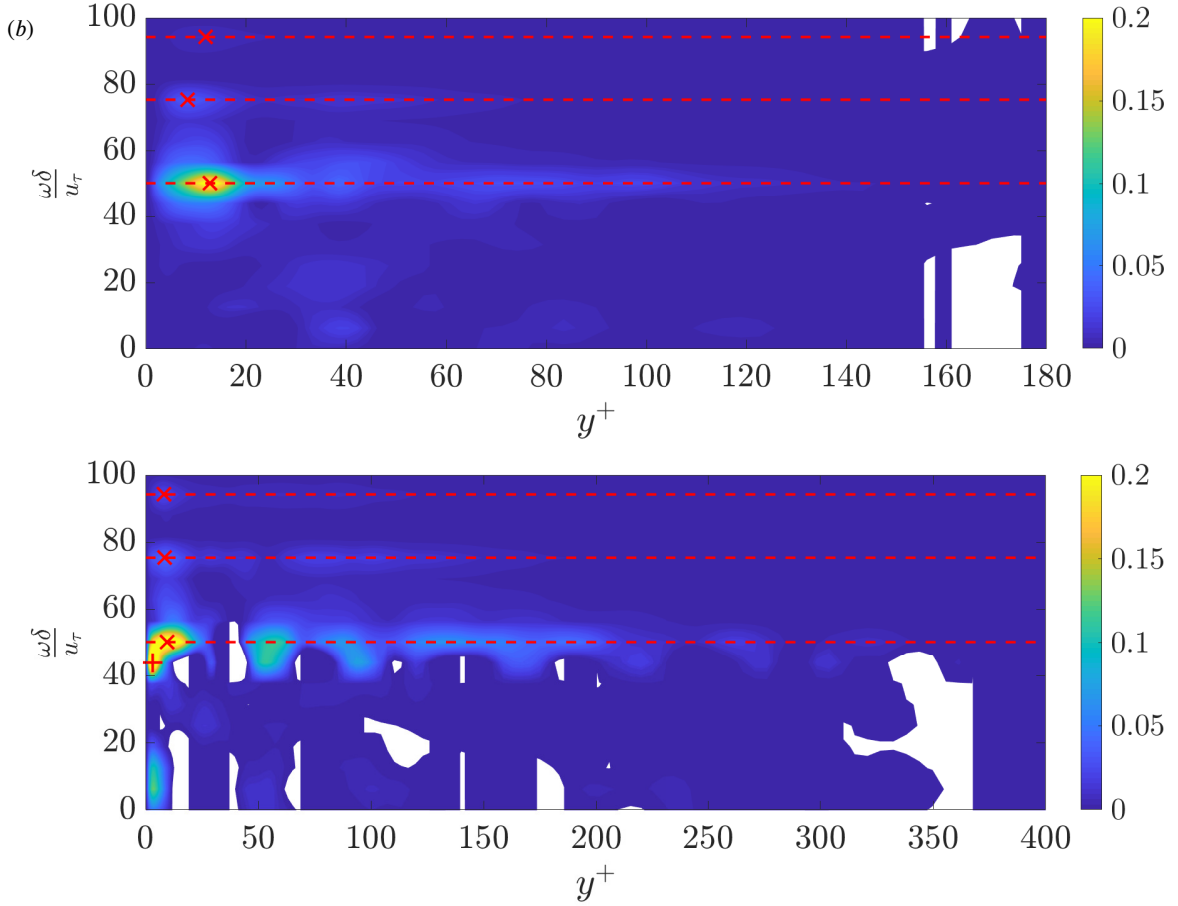


Figure 7: Real part of the normalized wall displacement-net displacement source CSD $\frac{Re(\Psi_a(y^+, \omega \delta / u_\tau))}{\int_{-\infty}^{+\infty} \int_0^{+2Re_\tau} \Psi_a(y^+, \omega \delta / u_\tau) dy^+ d\omega \delta / u_\tau}$ for (a) $Re_\tau = 180$ and (b) $Re_\tau = 400$. Contours are 100 equally spaced values between 0 and 0.2. Blank regions have negative value of $Re(\Psi^a)$. Horizontal dashed red lines denote the peak frequencies of the plate averaged displacement PSD. Red crosses indicate the wall-normal coordinate with maximum value of Ψ^a at the peak frequencies. Red plus in (b) indicates the location of global maximum of Ψ^a for $Re_\tau = 400$.

(Anantharamu and Mahesh, 2019) using the Green's function formulation,

$$\begin{aligned} \phi_{pp}(\omega) &= \iint_{-\delta}^{+\delta} \Gamma(r, s, \omega) dr ds, \\ \Gamma(r, s, \omega) &= \iint_{-\infty}^{+\infty} G^*(-\delta, r, k) G(-\delta, s, k) \varphi_f(r, s, k_1, k_3, \omega) dk_1 dk_3. \end{aligned} \quad (45)$$

where $\Gamma(r, s, \omega)$ is the net source CSD. Net source is a function $f_G(x, y, z, t)$ whose integral in the wall-normal direction gives the instantaneous wall-pressure fluctuation $p(x, -\delta, z, t) = \int_{-1}^{+1} f_G(x, y, z, t) dy$. Combining equations 18, 19,

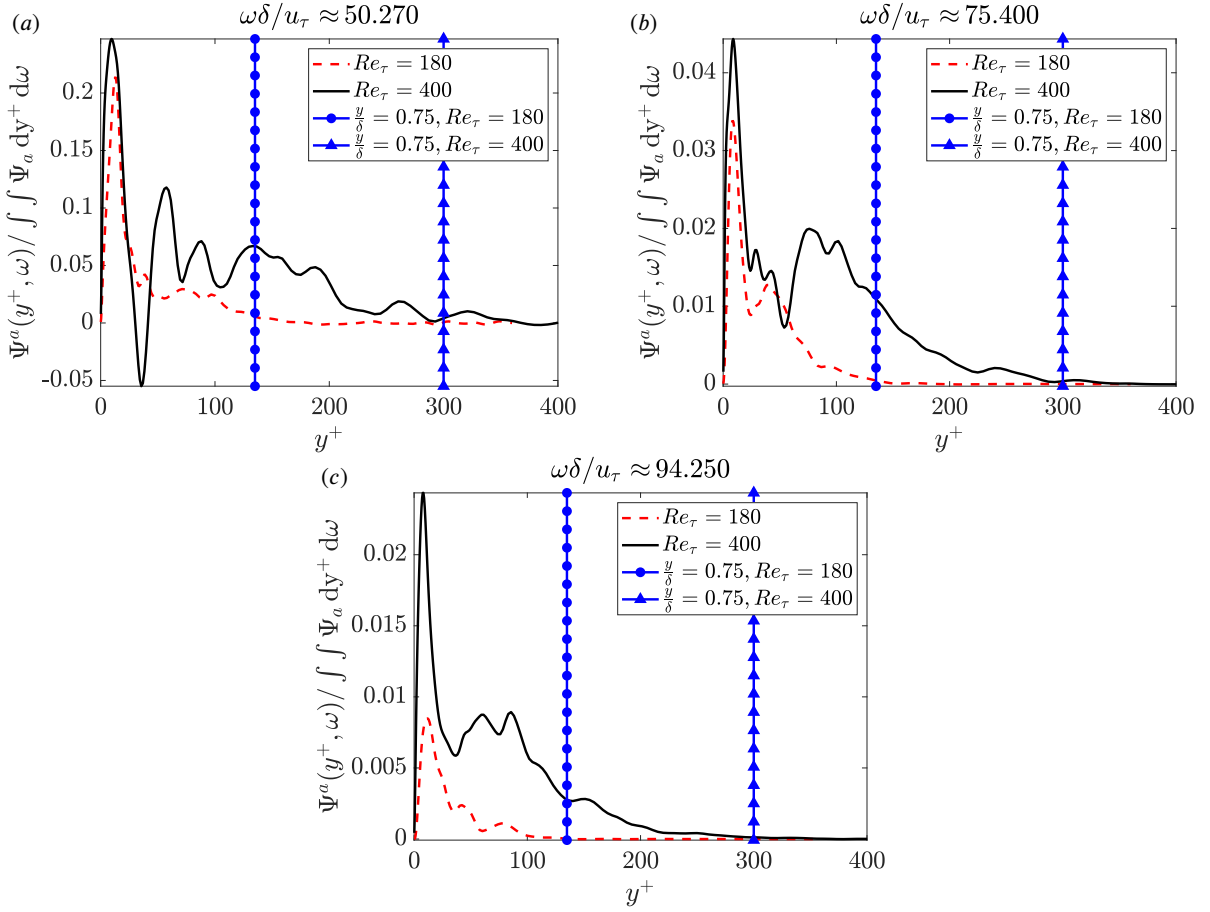


Figure 8: Comparison plate averaged wall displacement-net displacement source CSD (normalized by its integral) at the peak frequencies (a) $\omega\delta/u_\tau \approx 50.2$, (b) $\omega\delta/u_\tau \approx 75.4$ and (c) $\omega\delta/u_\tau \approx 94.25$ for $Re_\tau = 180$ (dashed red line) and $Re_\tau = 400$ (solid black line). Vertical dashed-dotted red and dotted black lines indicate $y/\delta = 0.5$ for $Re_\tau = 180$ and 400, respectively.

and 21 45, we obtain the desired result,

$$\begin{aligned} \phi_{dd}^a(\omega) &= \iint_{-\delta}^{+\delta} \Gamma^a(r, s, \omega) dr ds = \iint_{-\delta}^{+\delta} \Gamma(r, s, \omega) \alpha(\omega) dr ds, \\ \alpha(\omega) &= \iint_{-\infty}^{+\infty} A\left(\frac{k_1 U_c}{\omega}\right) B\left(\frac{k_3 U_c}{\omega}\right) \\ &\quad \left(\sum_{j=1}^{\infty} |\hat{H}_j(\omega)|^2 |S_j(k_1, k_3)|^2 \right) dk_1 dk_3. \end{aligned} \quad (46)$$

Note that $\alpha(\omega)$ is a positive number. Thus, for a Corcos type spectrum both plate averaged displacement PSD and wall-pressure PSD couple in a similar manner with the fluid sources.

5.3. Spectral POD of fluid sources

Before we present the spectral POD results of $\Gamma^a(r, s, \omega)$, we discuss the relevance of the spectral POD modes and eigenvalues to the plate surface displacement. Recall equation 4 that relates the surface displacement at a point (x, z) on the plate to the net displacement source,

$$d(x, -\delta, z, t) = \int_{-\delta}^{+\delta} f_d(x, y, z, t) dy. \quad (47)$$

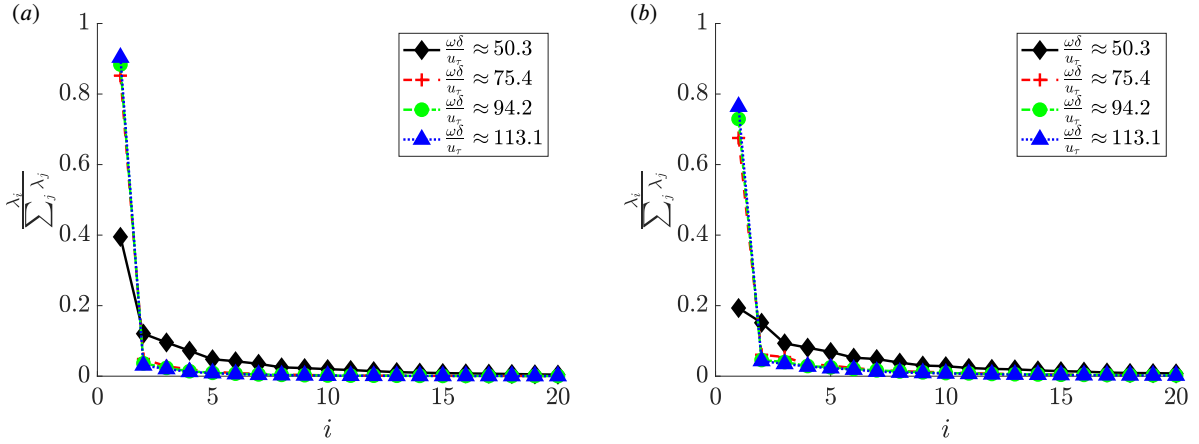


Figure 9: Spectral POD eigenvalues for a) $Re_\tau = 180$ and b) $Re_\tau = 400$ computed using the Poisson inner product ($\beta = 0.5$).

The Fourier transform of the net displacement source can be expanded in the spectral POD basis $\{\Phi_j^*\}_{j=1}^\infty$ as

$$\begin{aligned} f_d(x, y, z, t) &= \int_{-\infty}^{+\infty} \hat{f}(x, y, z, \omega) e^{i\omega t} d\omega, \\ &= \int_{-\infty}^{+\infty} \sum_{j=1}^{\infty} \alpha_j(x, z, \omega) \Phi_j^*(y, \omega) e^{i\omega t} d\omega, \end{aligned} \quad (48)$$

where $\{\alpha_j(x, z, \omega)\}_{j=1}^\infty$ are the coefficients of expansion of $\hat{f}_d(x, y, z, \omega)$. Using equation 48 in equation 47, and rearranging the integral, we have

$$d(x, -\delta, z, t) = \int_{-\infty}^{+\infty} \alpha_j(x, z, \omega) e^{i\omega t} \left(\int_{-\delta}^{+\delta} \Phi_j^*(y, \omega) dy \right) d\omega. \quad (49)$$

Using the expression $\Phi_j^*(y, \omega) = |\Phi_j(y, \omega)| e^{-\angle \Phi_j(y, \omega)}$ in the above equation, we have

$$d(x, -\delta, z, t) = \int_{-\infty}^{+\infty} \alpha_j(x, z, \omega) e^{i\omega t} \left(\int_{-\delta}^{+\delta} |\Phi_j(y, \omega)| e^{-\angle \Phi_j(y, \omega)} dy \right) d\omega. \quad (50)$$

The above equation expresses the plate displacement as sum of contributions from each spectral POD mode. Further, the coefficients $\{\alpha_j(x, z, \omega)\}_{j=1}^\infty$ are decorrelated in the plate averaged sense, i.e.,

$$\frac{1}{A_p} \int_{\Gamma_{fs}} \langle \alpha_j(x, z, \omega) \alpha_k(x, z, \omega_o) \rangle dx dz = \lambda_j(\omega) \delta_{jk} \delta(\omega - \omega_o), \quad (51)$$

where δ_{ij} is the Kronecker delta and δ is the Dirac Delta function. We include the effect of structures of all length scales because we integrate over all wavenumbers in equation 22.

We set the parameter β in the Poisson inner product (equation 23) to a small value of 0.5 to compute the spectral POD modes and eigenvalues. We did not observe a change in the computed mode shapes or eigenvalues for values smaller than 0.5. Further, we will see that the value $\beta = 0.5$ identifies a single dominant mode of the net displacement source responsible for the plate excitation.

Figures 9a and b show the computed spectral POD eigenvalues (normalized by the sum of eigenvalues) for both Re_τ at the first four peak frequencies in figure 4a. The eigenvalues decay faster with increasing frequency indicating that fewer modes are required to represent the double integral $\iint_{-1}^{+1} G(r, s, \beta/(1-\beta))/(1-\beta) \Gamma^a(r, s, \omega) dr ds$ (equation 27).

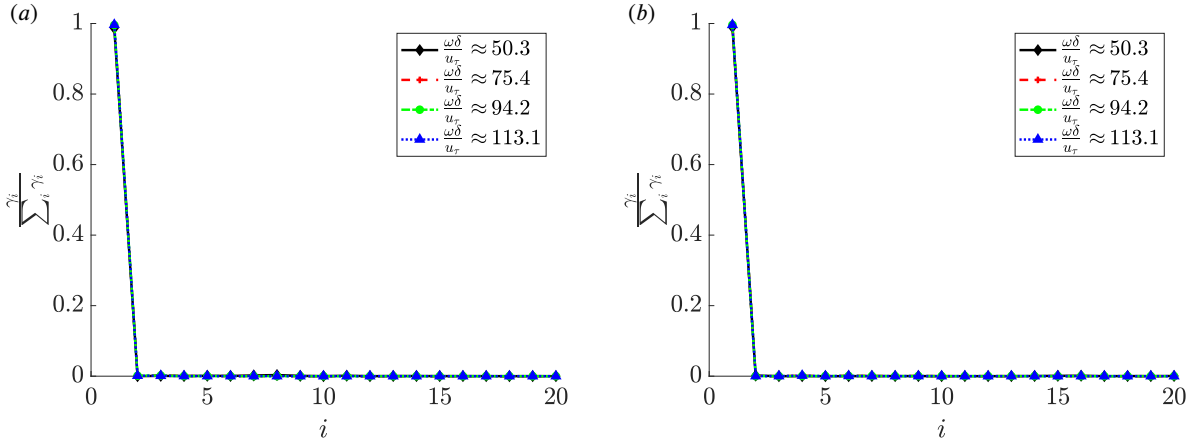


Figure 10: Contribution of each spectral POD mode to plate averaged displacement PSD for a) $Re_\tau = 180$ and b) $Re_\tau = 400$ computed using the Poisson inner product ($\beta = 0.5$).

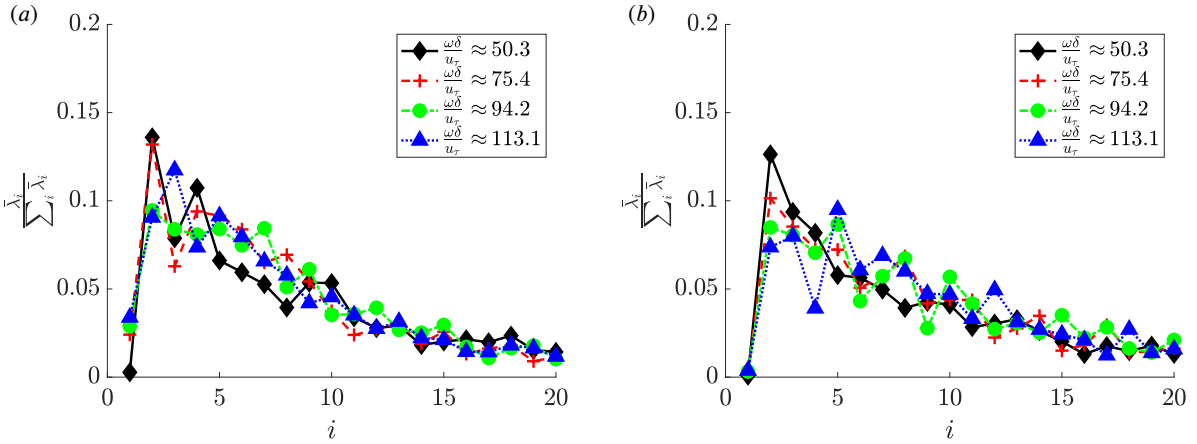


Figure 11: Contribution of each spectral POD mode computed using the Poisson inner product ($\beta = 0.5$) to the net displacement source PSD for a) $Re_\tau = 180$ and b) $Re_\tau = 400$. For definition of $\bar{\lambda}_i$, see equation 31

Figures 10a and b show the contribution of each spectral POD mode to the plate averaged displacement PSD (equation 28) for the frequencies plotted in figure 9. The first spectral POD mode contributes nearly all the plate averaged displacement PSD at all frequencies for both Re_τ . Thus, the first spectral POD mode is the dominant decorrelated contributor to plate response at all the peak frequencies. To investigate the structure of this dominant fluid source, we plot the envelope and phase of the first spectral POD mode in figures 12-15 for the frequencies plotted in figure 9. For all the Reynolds numbers and frequencies, the envelope is maximum in the buffer layer around $y^+ \approx 10$ and the modes have a similar wall-normal width for both Re_τ . This again reaffirms the observation in the previous section that the location and width of the dominant fluid source is in the buffer layer and depends on outer units, respectively. The phase variation of these dominant modes is mostly in the range $-\pi/2$ to $\pi/2$. Thus, the contribution from different wall-parallel planes interfere constructively. This constructive interference is absent in the suboptimal spectral POD modes. Even though the second spectral POD mode contains more energy than the first mode (figure 11), the contributions interfere destructively resulting in very small net contribution. Therefore, the interference of the contributions from different wall-parallel planes play a major role in determining the dominance of a spectral POD mode.

Figure 11 shows that the dominant spectral POD mode is not the dominant contributor to the integrated net displacement source PSD ($\int_{-\delta}^{+\delta} \Gamma^a(y, y, \omega) dy$), i.e., they are not energetically dominant. The first two energetically dominant modes identified by the inner product with $\beta = 1$ (standard L^2 inner product) is shown in figure 16 for $\omega\delta/u_\tau \approx 50$.

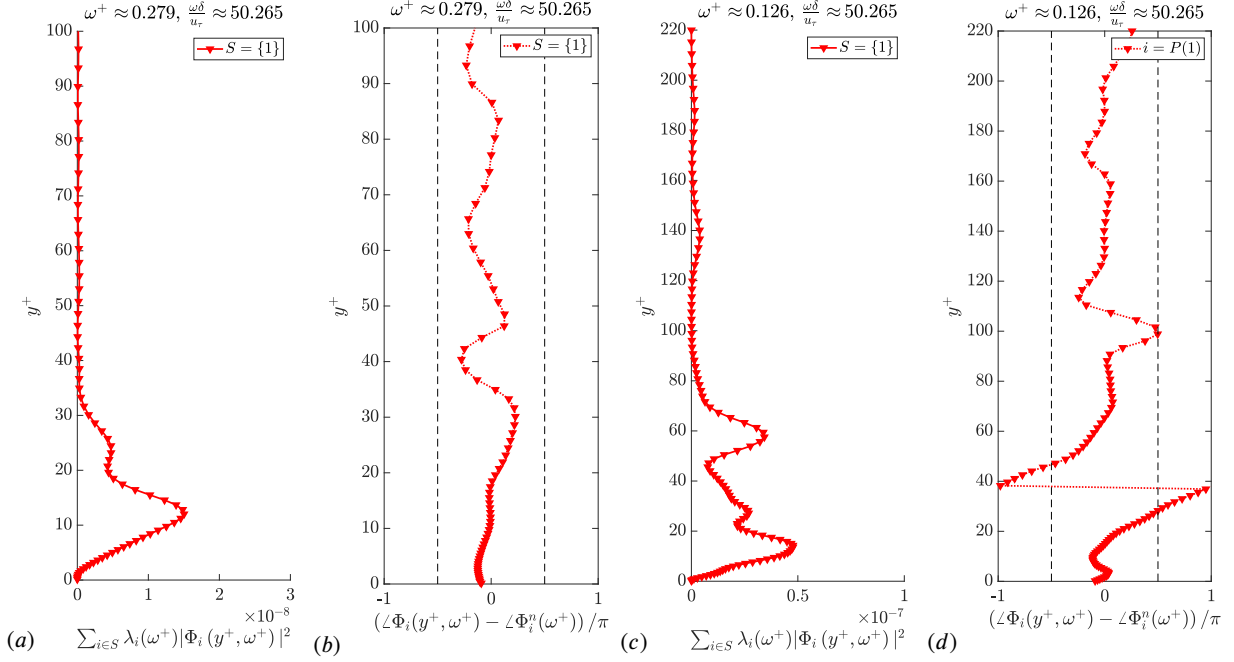


Figure 12: Envelope and phase of the dominant spectral POD mode computed using the Poisson inner product ($\beta = 0.5$) for $Re_\tau = 180$ ((a)-envelope, (b)-phase) and $Re_\tau = 400$ ((c)-envelope, (d)-phase) at peak frequency $\omega\delta/u_\tau \approx 50.2$.

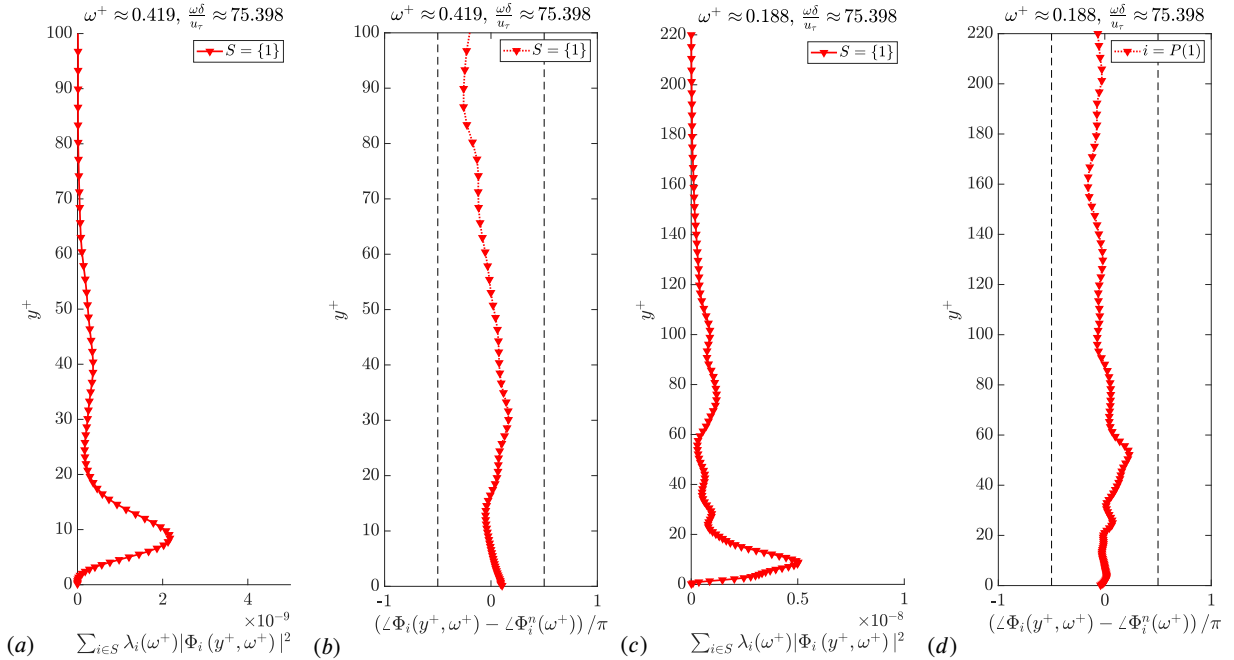


Figure 13: Envelope and phase of the dominant spectral POD mode computed using the Poisson inner product ($\beta = 0.5$) for $Re_\tau = 180$ ((a)-envelope, (b)-phase) and $Re_\tau = 400$ ((c)-envelope, (d)-phase) at peak frequency $\omega\delta/u_\tau \approx 75$.

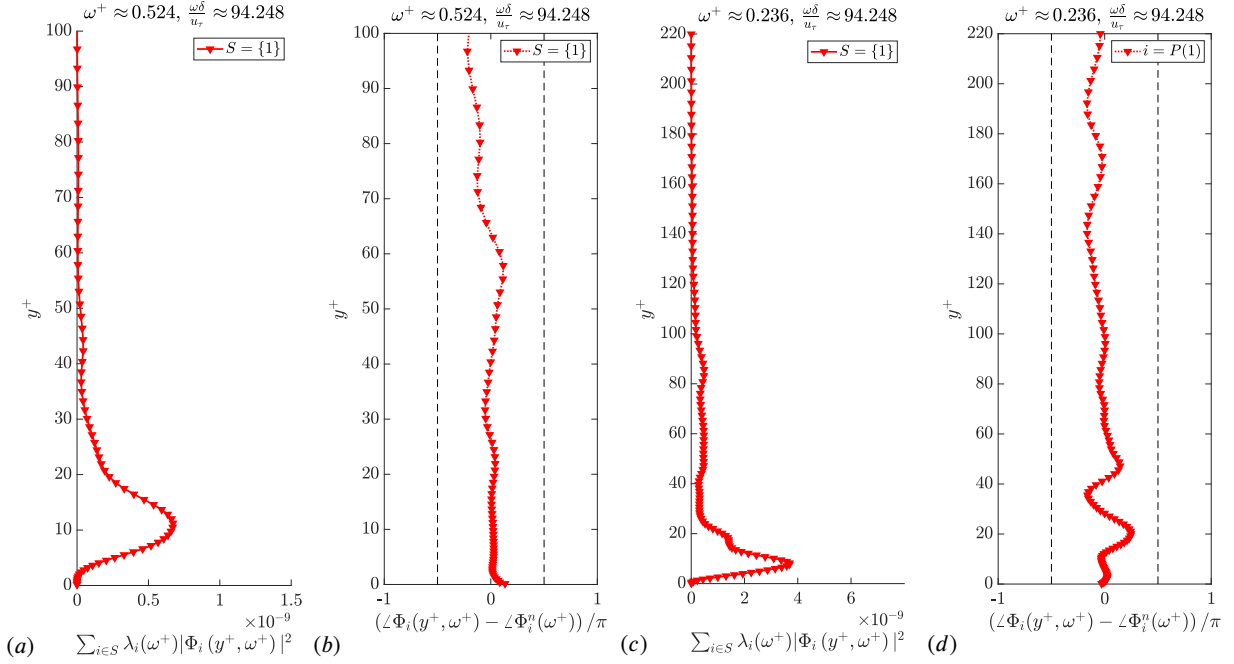


Figure 14: Envelope and phase of the dominant spectral POD mode computed using the Poisson inner product ($\beta = 0.5$) for $Re_\tau = 180$ ((a)-envelope, (b)-phase) and $Re_\tau = 400$ ((c)-envelope, (d)-phase) at peak frequency $\omega\delta/u_\tau \approx 94$.

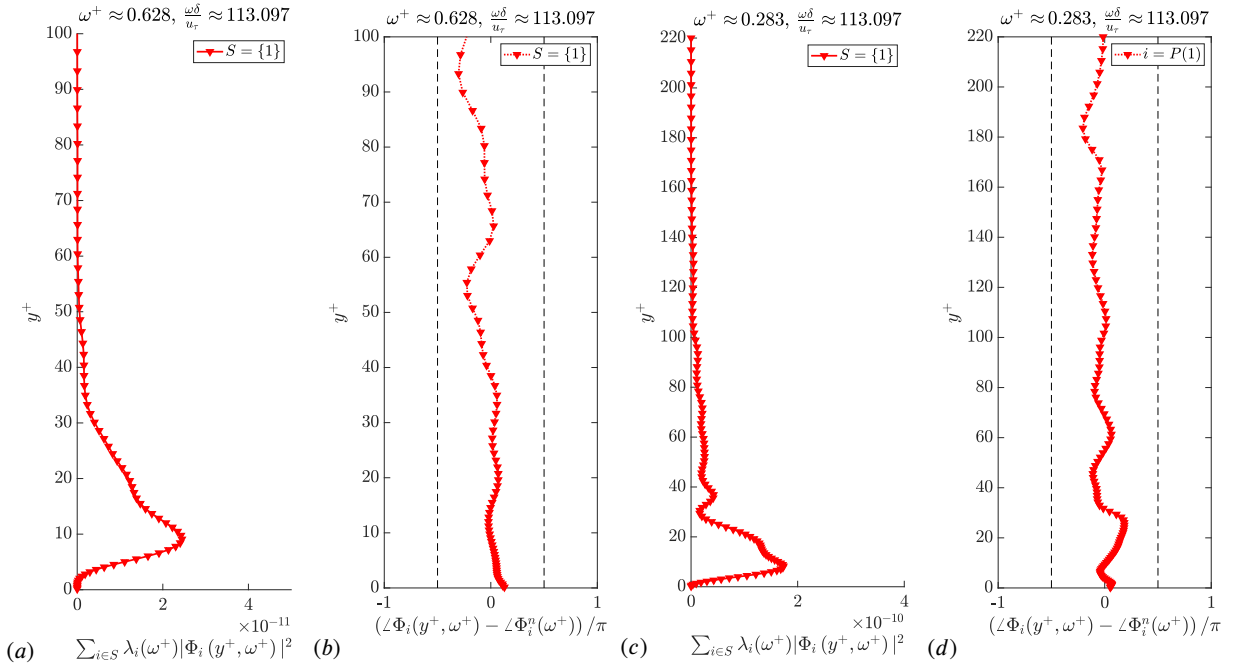


Figure 15: Envelope and phase of the dominant spectral POD mode computed using the Poisson inner product ($\beta = 0.5$) for $Re_\tau = 180$ ((a)-envelope, (b)-phase) and $Re_\tau = 400$ ((c)-envelope, (d)-phase) at peak frequency $\omega\delta/u_\tau \approx 113$.

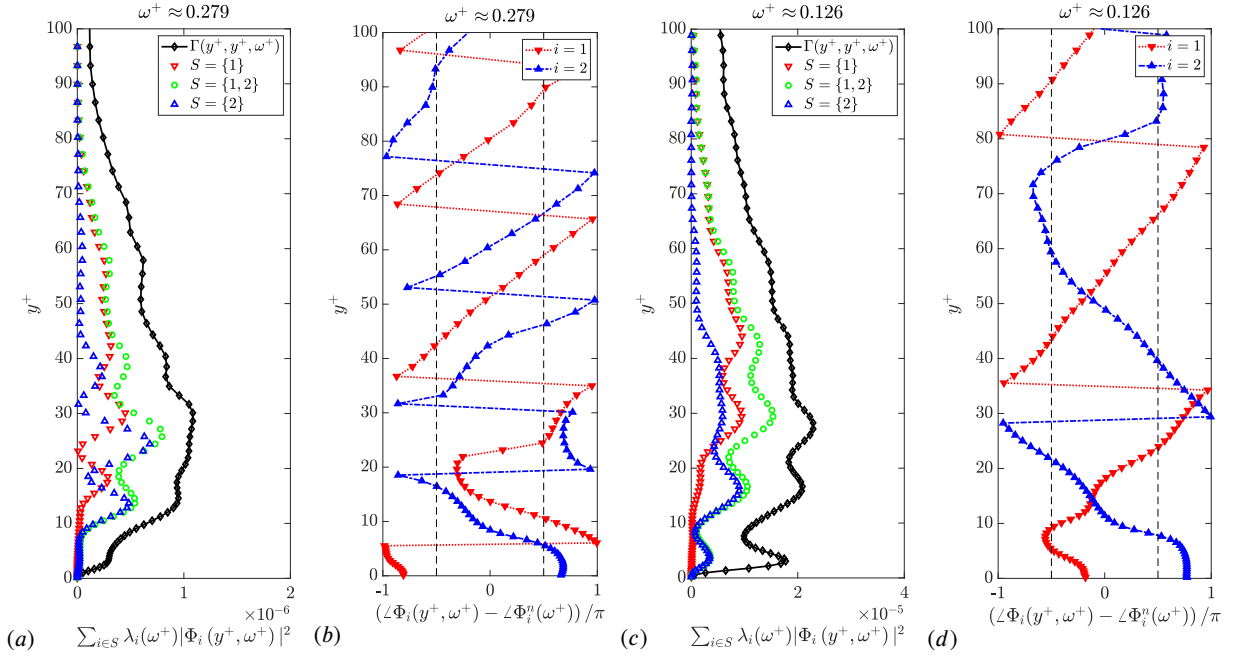


Figure 16: Envelope and phase of the dominant spectral POD modes computed using the L^2 inner product for $Re_\tau = 180$ ((a)-envelope, (b)-phase) and $Re_\tau = 400$ ((c)-envelope, (d)-phase) at peak frequency $\omega\delta/u_\tau \approx 50.2$.

The shape of the modes resemble a stationary wavepacket enclosing a travelling wave (almost linear phase variation) for both Re_τ . However, these wavepackets do not contribute much to the response of the plate as the contribution from different wall-normal locations interfere destructively to produce no net contribution. This behavior of the energetically dominant mode is also true at higher frequencies (not shown). Further, the spectral POD modes identified by the inner-products with $\beta = 1$ (standard L^2 inner-product) and $\beta = 0.5$ are inherently different because they optimize the modes based on their contribution to $\int_{-\delta}^{+\delta} \Gamma^a(y, y, \omega) dy$ and $\iint_{-\delta}^{+\delta} 2G(y, r, 1))\Gamma^a(r, y, \omega) dr dy$, respectively. The former picks the energetically dominant mode whereas the latter identifies the mode that contributes the most to the double integral (which is a proxy for $\phi_{dd}^a(\omega)$).

Overall, spectral POD identifies a single dominant contributor to the plate excitation at each of the first four peak frequencies of the plate averaged displacement PSD. All the identified dominant plate excitation modes have an envelope that has a peak in the buffer layer around $y^+ \approx 10 - 13$ and has a width that scales in outer units for the two Re_τ .

6. Summary

In summary, we present a novel framework to investigate the fluid-solid coupling in a canonical setting - linear one-way coupled excitation of an elastic plate in turbulent channel flow. We apply the framework to explain the response of a clamped plate obtained using the in-house FSI solver - MPCUGLES-SOLID at $Re_\tau = 180$ and 400.

The structural solver is first validated using the experiment of Han et al. (1999). They measured the response of a rectangular steel plate excited by a turbulent boundary layer at $Re_\tau \approx 2000$. We generate synthetic space-time wall-pressure fluctuations at the experimental conditions using a Fourier series methodology. The generated fluctuations satisfy the Corcos CSD and Smolyakov-Tkachenko PSD models. To compute the surface forces accurately and efficiently, we perform L^2 orthogonal projection of the generated wall-pressure fluctuations onto the Legendre polynomial basis within each surface element of the plate. The obtained time-domain FEM response of the plate shows good agreement with the measured velocity PSD at a point on the plate.

The obtained plate response at $Re_\tau = 180$ and 400 with fixed non-dimensional Young's modulus $E/(\rho_f u_\tau^2)$ have overlapping plate averaged low frequency spectrum in outer units. But, the high frequency component of the spectrum

does not show overlap in inner units. Fixing $E\delta^2/(\rho_f v^2)$ instead of $E/(\rho_f u_\tau^2)$ for the two Re_τ yields a better collapse of the high-frequency region in inner units. We show that this high-frequency behavior is due to the inner scaling of the modal wavenumber of the plate.

In the proposed fluid-solid coupling framework, we express the displacement at a point on the surface of the plate $d(x, -1, z, t)$ as a wall-normal integral of the net displacement source $f_d(x, y, z, t)$, i.e., $d(x, -\delta, z, t) = \int_{-\delta}^{+\delta} f_d(x, y, z, t) dy$. To quantify the statistical features of fluid sources of plate excitation, we compute the plate averaged CSD of the net displacement source using the DNS database and modal superposition. We use the first six mode shapes of the plate to investigate the fluid sources responsible for the first four peaks of the plate averaged displacement spectra. The computed plate averaged WD-NDS CSD $\Psi^a(y, \omega)$ shows a dominant buffer layer contribution at the peak frequencies of the plate averaged displacement PSD. The CSD has large values for $y/\delta < 0.75$ indicating that the width of the fluid source depends on outer units. Further, we show that the Corcos form of the wavenumber frequency spectrum implies identical coupling of the plate averaged displacement PSD and the wall-pressure PSD with the fluid sources in the channel upto a multiplicative constant.

We perform spectral POD of the net displacement source CSD to identify the decorrelated dominant fluid sources responsible for the plate excitation. To accomplish this, we require the modes to be orthogonal in a Poisson inner product (with $\beta = 0.5$ instead of the commonly used L^2 inner product). The envelope of the dominant spectral POD mode (obtained with $\beta = 0.5$) peaks in the buffer region around $y^+ \approx 10 - 13$ for both Re_τ and the width of the envelope scales in outer units. This reaffirms the previous observation that the location and wall-normal width of the dominant source is a function of inner and outer units, respectively. The dominance of such a fluid source is mainly due to the constructive interference of the contributions from different wall-parallel planes. However, this dominant contribution to plate excitation is not energetically dominant. The energetically dominant fluid sources obtained from spectral POD with the L^2 inner product ($\beta = 1$) resemble stationary wall-normal wave packets. But these wavepackets do not contribute much to the plate response as the contribution from different wall-normal locations to the plate response undergo destructive interference.

Overall, the buffer region sources are dominant contributors to plate excitation. In FSI simulations that use wall-modeled Large Eddy Simulation (LES) in the fluid domain, the first point in the fluid domain will be in the logarithmic layer. Thus, wall-modeling will fail to account for this dominant buffer region contribution. With increasing Reynolds numbers, the contribution of the outer layer structures to the wall-pressure fluctuation increases (Panton et al. (2017)). The proposed framework can be used to quantitatively investigate this outer layer contribution to the plate excitation. Further, due to the dominance of the buffer layer structures, modulating the buffer region can be a possible way to control structural excitation.

Acknowledgements

This work is supported by the United States Office of Naval Research (ONR) under grant N00014-17-1-2939 with Dr. Ki-Han Kim as the technical monitor. The computations were made possible through computing resources provided by the US Army Engineer Research and Development Center (ERDC) in Vicksburg, Mississippi on the Cray machines, Copper and Onyx of the High Performance Computing Modernization Program. We also thank for the computing resources provided by the US Air Force Research Laboratory DoD Supercomputing Resource Center (DSRC) on the SGI ICE machine, Thunder of the High Performance Computing Modernization Program.

A. Surface force evaluation for validation

In FEM, the integral to compute the surface force at a typical boundary node i in a boundary element e is

$$\int_{\Gamma_e} p(x, -1, z, t) N_i(x, z) dx dz, \quad (52)$$

where Γ_e is the boundary surface of element e and N_i is the shape function of the node i . The cost of computing this integral exactly using the standard Gauss-Legendre quadrature is high because i) the generated $p(x, -1, z, t)$ consists of ≈ 1 billion terms and ii) the order of quadrature rule to exactly integrate the high wavenumber component of the generated wall-pressure fluctuations is high. To reduce this high cost, we write the projected pressure fluctuation $\overline{p(x, -1, z, t)}$ within each surface element in the Legendre polynomial basis, i.e., $\overline{p(x, -1, z, t)}|_{\Gamma_e} = \sum_{j,k=0}^2 \alpha_{j,k}^e(t) P_j(x) P_k(z)$, where

$\{P_j\}_{j=0}^2$ is the set of Legendre polynomials of degree ≤ 2 . To find the coefficients $\{\alpha_{j,k}(t)\}_{j,k=0}^2$, we require the error in projection of $p(x, -1, z, t)$ (equation 2) to be orthogonal to polynomials of degree 2, i.e.,

$$\int_{\Gamma_e} \left(p(x, -1, z, t) - \overline{p(x, -1, z, t)} \Big|_{\Gamma_e} \right) P_j(x) P_k(z) dx dz = 0; j, k = 0, 1, 2. \quad (53)$$

We can show that the expression for $\alpha_{j,k}^e(t)$ is

$$\alpha_{j,k}^e(t) = \sum_{n=-N_x^f/2}^{N_x^f/2-1} \left(\sum_{l=-N_x^f/2}^{N_x^f/2-1} \sum_{m=-N_z^f/2}^{N_z^f/2-1} \hat{p}_{l,m,n} \beta_{j,k}^{e,l,m} \right) e^{i\omega_n t}, \quad (54)$$

where $\beta_{j,k}^{e,l,m}$ is the coefficient of the projection of $e^{i(k_l x + k_m z)}$, i.e.,

$$\overline{e^{i(k_l x + k_m z)}} \Big|_{\Gamma_e} = \sum_{j,k=0}^2 \beta_{j,k}^{e,l,m} P_j(x) P_k(z), \quad (55)$$

We define $\overline{e^{i(k_l x + k_m z)}} \Big|_{\Gamma_e}$ by replacing $p(x, -1, z, t)$ in equation 53 by $e^{i(k_l x + k_m z)}$. For implementation details, see appendix. We use the obtained $\overline{p(x, -1, z, t)} \Big|_{\Gamma_e}$ to compute the surface force instead of $p(x, -1, z, t)$ since

$$\int_{\Gamma_e} p(x, -1, z, t) N_i(x, z) dx dz = \int_{\Gamma_e} \overline{p(x, -1, z, t)} \Big|_{\Gamma_e} N_i(x, z) dx dz. \quad (56)$$

The above equality holds since we can express $N_i(x, z)$ as a combination of the polynomial basis functions $\{P_i(x)P_k(z)\}_{i,k=0}^2$ used to perform the projection (equation 53). Such an expression for $N_i(x, z)$ is possible because i) the surface element is a Cartesian domain, and ii) the degree of polynomial used to represent the FEM solution is less than or equal to the degree of the polynomial used to perform the above projection.

References

- Anantharamu, S., Mahesh, K., 2019. Analysis of wall-pressure fluctuation sources from DNS of turbulent channel flow. Under review in Journal of Fluid Mechanics (arXiv preprint arXiv:1911.08534v2).
- Bathe, K.J., 2006. Finite element procedures. Klaus-Jurgen Bathe.
- Bendat, J.S., Piersol, A.G., 2011. Random data: analysis and measurement procedures. volume 729. John Wiley & Sons.
- Bernardini, M., Pirozzoli, S., Quadrio, M., Orlandi, P., 2013. Turbulent channel flow simulations in convecting reference frames. Journal of Computational Physics 232, 1–6.
- Blake, W.K., 2017. Mechanics of Flow-Induced Sound and Vibration, Volume 1 and 2. Academic Press.
- Bull, M.K., 1967. Wall-pressure fluctuations associated with subsonic turbulent boundary layer flow. Journal of Fluid Mechanics 28, 719–754.
- Chang III, P.A., Piomelli, U., Blake, W.K., 1999. Relationship between wall pressure and velocity-field sources. Physics of Fluids 11, 3434–3448.
- Chase, D.M., 1980. Modeling the wavevector-frequency spectrum of turbulent boundary layer wall pressure. Journal of Sound and Vibration 70, 29–67.
- Corcos, G.M., 1964. The structure of the turbulent pressure field in boundary-layer flows. Journal of Fluid Mechanics 18, 353–378.
- Farabee, T.M., Casarella, M.J., 1991. Spectral features of wall pressure fluctuations beneath turbulent boundary layers. Physics of Fluids A: Fluid Dynamics 3, 2410–2420.
- Ghaemi, S., Scarano, F., 2013. Turbulent structure of high-amplitude pressure peaks within the turbulent boundary layer. Journal of Fluid Mechanics 735, 381–426.
- Goody, M., 2004. Empirical spectral model of surface pressure fluctuations. AIAA Journal 42, 1788–1794.
- Hambric, S.A., Hwang, Y.F., Bonness, W.K., 2004. Vibrations of plates with clamped and free edges excited by low-speed turbulent boundary layer flow. Journal of Fluids and Structures 19, 93–110.
- Han, F., Bernhard, R.J., Mongeau, L.G., 1999. Prediction of flow-induced structural vibration and sound radiation using energy flow analysis. Journal of Sound and Vibration 227, 685–709.
- Hoyas, S., Jiménez, J., 2006. Scaling of the velocity fluctuations in turbulent channels up to $Re = 2003$. Physics of fluids 18, 011702.
- Hu, Z., Morfey, C.L., Sandham, N.D., 2006. Wall pressure and shear stress spectra from direct simulations of channel flow. AIAA Journal 44, 1541–1549.
- Hwang, Y.F., 1998. A discrete model of turbulence loading function for computation of flow-induced vibration and noise, in: Proceedings of the ASME International Mechanical Engineering Congress and Exposition, Anaheim, CA.

- Hwang, Y.F., Maidanik, G., 1990. A wavenumber analysis of the coupling of a structural mode and flow turbulence. *Journal of Sound and Vibration* 142, 135–152.
- Klöppel, T., Gee, M.W., Wall, W.A., 2011. A scaled thickness conditioning for solid-and solid-shell discretizations of thin-walled structures. *Computer Methods in Applied Mechanics and Engineering* 200, 1301–1310.
- Mahesh, K., Constantinescu, G., Moin, P., 2004. A numerical method for large-eddy simulation in complex geometries. *Journal of Computational Physics* 197, 215–240.
- Maxit, L., 2016. Simulation of the pressure field beneath a turbulent boundary layer using realizations of uncorrelated wall plane waves. *The Journal of the Acoustical Society of America* 140, 1268–1285.
- Panton, R.L., Lee, M., Moser, R.D., 2017. Correlation of pressure fluctuations in turbulent wall layers. *Physical Review Fluids* 2, 094604.
- Pope, S.B., 2001. *Turbulent flows*. Cambridge University Press.
- Powell, M.J.D., 1981. *Approximation theory and methods*. Cambridge university press.
- Rogallo, R.S., 1981. Numerical experiments in homogeneous turbulence .
- Rosti, M.E., Brandt, L., 2017. Numerical simulation of turbulent channel flow over a viscous hyper-elastic wall. *Journal of Fluid Mechanics* 830, 708–735.
- Schlichting, H., 1979. *Boundary-layer theory*, in: *Boundary-layer theory*. McGraw-Hill.
- Smol'IAkov, A.V., Tkachenko, V.M., 1991. Models of a field of pseudoacoustic turbulent wall pressures and experimental data. *Akusticheskii Zhurnal* 37, 1199–1207.
- Zhang, C., Wang, J., Blake, W., Katz, J., 2017. Deformation of a compliant wall in a turbulent channel flow. *Journal of Fluid Mechanics* 823, 345–390.